



Quantifying the potential of using SMAP soil moisture variability to predict subsurface water dynamics

Aruna Kumar Nayak¹, Xiaoyong Xu^{1,2}, Steven K. Frey^{3,4}, Omar Khader^{3,5}, Andre R. Erler³, David R. Lapen⁶, Hazen A.J. Russell⁷, and Edward A. Sudicky^{3,4}

- 5 ¹Department of Chemical and Physical Sciences, University of Toronto Mississauga, Mississauga, ON, Canada
²Department of Geography, Geomatics and Environment, University of Toronto Mississauga, Mississauga, ON, Canada
³Aquanty, Waterloo, ON, Canada
⁴Department of Earth and Environmental Sciences, University of Waterloo, Waterloo, ON, Canada
10 ⁵Department of Water and Water Structural Engineering, Zagazig University, Al Sharqia, Egypt
⁶Agriculture and Agri-Food Canada, Ottawa Research and Development Centre, Ottawa, ON, Canada
⁷Natural Resources Canada, Ottawa, ON, Canada

Correspondence to: Xiaoyong Xu (xiaoyong.xu@utoronto.ca)

Abstract. Advances in satellite Earth observation have opened up new opportunities for a global monitoring of soil moisture (SM) at fine to medium resolution, but satellite remote sensing can only measure the near-surface soil moisture (SSM). As
15 such, it is critically important to examine the potential of satellite SSM measurements to derive the water resource variations in deeper subsurface. This study compares the SSM variability captured by the Soil Moisture Active and Passive (SMAP) satellite and the Soil Water Index (SWI) derived from SMAP SSM with subsurface SM and groundwater (GW) dynamics simulated by a high resolution fully-integrated surface water - groundwater model over an agriculturally-dominated watershed in eastern Canada across two spatial scales, namely SMAP product grid (9 km) and watershed (~4000 km²).
20 SMAP measurements compare well with the hydrologic simulations in terms of SSM variability at both scales. Simulated subsurface SM and GW storage show lagged and smoother characteristics relative to SMAP SSM variability with an optimal delay of ~1 days for the 25–50 cm SM, ~6 days for the 50–100 cm SM, and ~11 days for the GW storage for both scales. Modelled subsurface SM dynamics agree well with the SWI derived from SMAP SSM using the classic characteristic time lengths (15 days for the 0–25 cm layer and 20 days for the 0–100 cm layer). The simulated GW storage showed a slightly
25 delayed variation relative to the derived SWI. The quantified optimal characteristic time length T_{opt} for SWI estimation (by matching the variations in SMAP-derived SWI and modeled root zone SM) is comparable to T_{opt} obtained in other agricultural regions around the world. This work demonstrates SMAP SM measurements as a potentially useful aid when predicting root zone SM and GW dynamics and validating fully integrated hydrologic models across different spatial scales. This study also provides insights into the dynamics of near surface–subsurface water interaction and the capabilities and
30 approaches of satellite-based SM monitoring and high resolution fully-integrated hydrologic modelling.



1 Introduction

Accurate information on soil moisture (SM) and groundwater (GW) storage is essential for assessing water resources and making informed decisions for effective water resource management. SM can be monitored and measured using ground-based in situ sensor networks and remote sensing methods (e.g., Dobriyal et al., 2012). The in situ SM monitoring networks are able to provide continuous measurements for different soil depths or profiles; however, the monitoring sites are typically sparse, especially at continental or global scales, causing difficulty in large-scale spatially distributed SM estimation (e.g., Jonard et al., 2018; Singh et al., 2019). Advances in satellite Earth observation have opened up opportunities for the large-scale and global monitoring of SM at fine to medium resolution (e.g., Bartalis et al., 2007; Entekhabi et al., 2010; Kerr et al., 2010; Njoku et al., 2003; Owe et al., 2008; Xu et al., 2014), but satellite remote sensing only measures the near-surface soil layer (the topmost few centimeters) and cannot directly observe the deeper soils. Further, NASA's Gravity Recovery and Climate Experiment (GRACE) and GRACE-Follow On (GRACE-FO) have made it possible to track changes in terrestrial water storage (TWS) by detecting Earth's gravitational changes (Tapley et al., 2004). The TWS observations, in combination with model outputs or reanalysis products, can be used to quantify GW storage dynamics (Famiglietti et al., 2011; Rodell et al., 2007, 2009, 2018; Syed, et al., 2008; Thomas and Famiglietti, 2019; Zhu et al., 2022). However, the coarse-scale (a native resolution of ~3 degrees in both latitude and longitude) monthly TWS changes provided by the GRACE/GRACE-FO observations cannot fully meet the needs for monitoring the variations in GW across different temporal and spatial scales.

As such, the potential of satellite near-surface soil moisture (SSM) measurements for estimating or predicting the variations in root zone SM and GW has received considerable attention over the past decades (e.g., Bouaziz et al., 2020; Ceballos et al., 2005; Ford et al., 2014; Nayak et al., 2021; Paulik et al., 2014; Sutanudjaja et al., 2013; Tian et al., 2020; Wagner et al., 1999; Zhao et al., 2008). One of the key steps for this important application is identification of the coupling strength and the associated temporal differences in response to wetting/drying processes among different subsurface layers, which can vary remarkably across different regions and different time windows depending on a suite of factors, such as depths considered, soil hydraulic properties, soil texture, climate conditions, and land cover (e.g., Albergel et al., 2008; Bouaziz et al., 2020; Wang et al., 2017).

The differences in responses to wetting/drying processes in the soil profile can be examined using in situ measurements (e.g., Mahmood et al., 2012; Wu et al., 2002) or hydrological models (e.g., Mahmood and Hubbard, 2007). The time lagged cross-correlation in SM variations identified between the surface and deeper soil layers (e.g., Mahmood and Hubbard, 2007; Mahmood et al., 2012; Wu et al., 2002) may indicate that the deeper subsurface SM variability could be approximated by delaying the temporal variations in SSM. On the other hand, the deeper subsurface soil water content can be estimated by smoothing the SSM time series since soil water in the deeper layers typically exhibit smaller variations and longer response times to critical precipitation/drying events that occur at the surface (e.g., Albergel et al., 2008; Manfreda et al., 2014;



Ragab, 1995; Wagner et al., 1999). A widely used smoothing method is the Soil Water Index (SWI) that estimates the
65 subsurface SM profiles from the SSM time series using an exponential filter with the characteristic time length T as the only
control parameter (Wagner et al., 1999). The optimal characteristic time length (T_{opt}) can be obtained by matching the SWI
to reference root zone SM (e.g., Bouaziz et al., 2020; Ceballos et al., 2005; Ford et al., 2014; Paulik et al., 2014; Tian et al.,
2020; Wagner et al., 1999).

70 Over the past decades, land surface and hydrological models have played an important role in quantifying T_{opt} for SWI
estimation. Albergel et al. (2008) investigated the effects of various factors on T_{opt} for SWI estimation by a combined use of
in situ and model data for soils in France. Wang et al. (2017) demonstrated the capability of vadose zone model simulations
in quantifying the relationships between T_{opt} and its various influencing factors (precipitation, land cover, and soil hydraulic
properties) over the continental United States. Bouaziz et al. (2020) utilized the root zone SM simulated by a process-based
75 lumped hydrological model as reference to quantify T_{opt} values for SWI estimation from different satellite SM products
across a number of watersheds in France. In addition, the inter-comparisons between satellite SM and modeled SM data have
received intensive research efforts (e.g., Al-Yaari et al., 2014; Dorigo et al., 2010; Draper et al. 2013; Parrens et al., 2012).

Recent advances in high resolution fully-integrated surface water-groundwater modeling for Canadian basins (Erler et al.,
80 2019; Frey et al., 2021; Xu et al., 2021; Aziz et al., 2023) have provided new opportunities for simulating water dynamics in
the variably-saturated subsurface domain. Such models present better ability to reproduce realistic root zone SM and GW
dynamics than surface-water models used in previous studies. Hence, these models are well suited to help expand our
understanding of connections between satellite SM and the variably-saturated subsurface flow regime. Accordingly, this
study aims to advance our understanding of: i) the coupling and response time differences between satellite SM dynamics
85 and transient soil water and groundwater storage characteristics, ii) the dependence of coupling and response time
differences on spatial scale, iii) the ability of state-of-the-art satellite SM monitoring to predict root zone SM and GW
dynamics, and iv) the ability of satellite SM data to assist with validation of large-scale integrated hydrologic models. To this
end, the study herein examines the linkages between the Soil Moisture Active Passive (SMAP) SM, which represents one of
90 the state-of-the-art satellite-based SM products, and the subsurface SM and GW dynamics simulated by a high-resolution
fully-integrated surface water-groundwater model of an agriculture-dominated watershed across two spatial scales, namely
SMAP 9-km grid cell and watershed.

2 Data and Methods

2.1 Study Watershed

The study domain is the South Nation Watershed (SNW) in eastern Ontario, Canada (Fig. 1a). The SNW is an agriculture-
95 dominated, mixed use watershed with an areal coverage of about 3900 km² (Figure 1b).

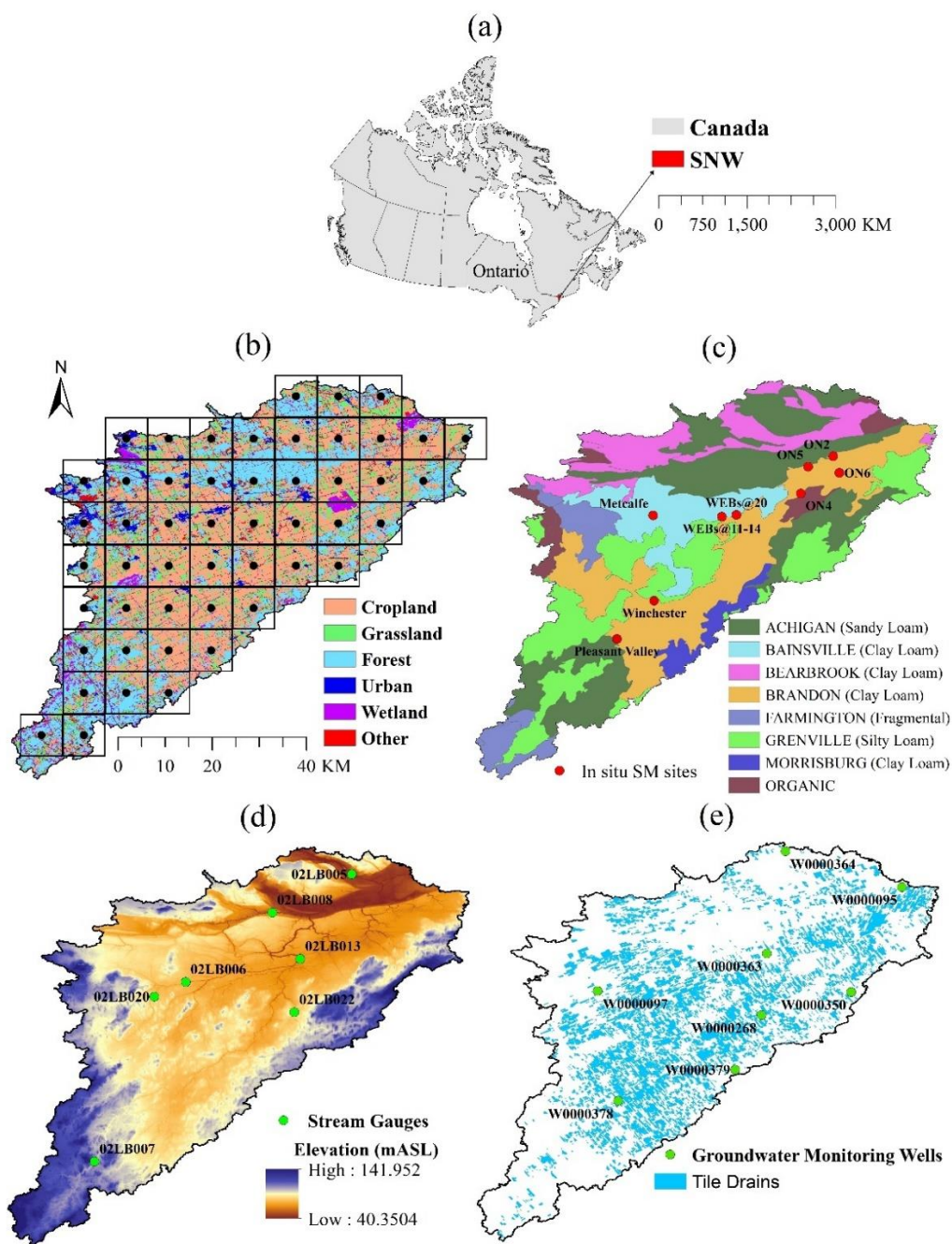


Figure 1: (a) Location of the South Nation Watershed (SNW). (b) The SNW land cover map (source: Agriculture and Agri-Food Canada’s Annual Crop Inventory 2015) overlaid with location of the 9-km grids (boxes for the pixels and black dots for the centers) for the SMAP SM product used in this study. (c) Soil map for the SNW (source: Soil Landscapes of Canada version 3.2, Agriculture and Agri-Food Canada), along with the in situ SM monitoring sites. (d) Surface elevation along with location of streamflow gauges. (e) Tile drains installed for the SNW (provided by the South Nation Conservation Authority), along with location of groundwater level monitoring wells.

100



The major crop types grown in the area are corn and soybeans. In the agricultural fields, natural soil water drainage is typically slow on account of extensive clay loam soil (Fig. 1c). The agricultural region generally has low topographic relief (Fig. 1d), with artificial subsurface drainage (tile drains) to drain excess water from fields to facilitate crop productivity (Fig. 1e). The tile drains tend to be spaced about 15 to 17 meters apart (Sunohara, et al., 2015), with a total tile-drained area of 956 km² (about 25% of the watershed). The watershed is characterized as having a humid temperate climate, and twenty-year (1998–2017) average annual precipitation is about 1000 mm, and average annual evapotranspiration is about 600 mm. The average water table is 1 to 3 meters below surface across much of the agricultural landscape.

2.2 Satellite SSM and SWI

For this study, satellite-based SM retrievals are taken from the SMAP enhanced L3 radiometer 9 km EASE-grid SM (SPL3SMP_E) version 5 product (O'Neill et al., 2021). The SPL3SMP_E product provides daily composite estimates of near-surface (~ top 5 cm) SM at a resolution of 9 km, retrieved from the AM (descending half orbits) and PM (ascending half orbits) brightness temperatures observed by the SMAP radiometer. In this study, only the SPL3SMP_E AM retrievals are used since the AM product is superior to the PM product over the study region, which is consistent with the AM/PM product comparison over the Great Lakes region (Xu, 2020). The location of the SPL3SMP_E product 9-km grid cells over the SNW is illustrated in Fig. 1b. A filtering step (using the SMAP product's ancillary information) was conducted to remove the SMAP SM estimates that were affected by various adverse factors (e.g., open water, frozen surfaces, snow, rain, or radio frequency interference). This study uses the SMAP SM data between March 31, 2015 (the date when SMAP started operation) and December 31, 2017, which is the time span overlapping with the temporal coverage of model simulations used in this work (section 2.3).

The SMAP SSM can be used to derive the moisture content in the deeper layers or entire unsaturated root zone with the SWI approach, which estimates the subsurface SM as a function of SSM utilizing an exponential filter (Wagner et al., 1999). The SWI method considers a near-surface soil layer and a subsurface layer. A water-balance approach is then applied to the two soil layers to compute the water fluxes across them, which are assumed to be proportional to their SM differences. In this study, we use the recursive exponential filter (Albergel et al., 2008), which is suitable for SWI estimation from the SSM observed at irregular time intervals. The SWI at time t_i is given by Eq. (1):

$$\text{SWI}(t_i) = \text{SWI}(t_{i-1}) + K(t_i) (\text{SSM}(t_i) - \text{SWI}(t_{i-1})), \quad (1)$$

where $\text{SWI}(t_i)$ and $\text{SWI}(t_{i-1})$ denote the SWI values at time t_i and t_{i-1} , respectively; $\text{SSM}(t_i)$ represents the SMAP near-surface soil moisture at time t_i ; and $K(t_i)$ is the gain at time t_i , which is given in a recursive form as in Eq. (2):

$$K(t_i) = \frac{K(t_{i-1})}{K(t_{i-1}) + \exp\left(\frac{-(t_i - t_{i-1})}{T}\right)}, \quad (2)$$



where $K(t_{i-1})$ is the gain at time t_{i-1} . The gain K ranges from 0 to 1 with the initialization $K(t_0) = 1$, while SWI is
135 initialized using the SSM series, i.e., $SWI(t_0) = SSM(t_0)$. The parameter T is the characteristic time length in days, and can
be considered as a surrogate for many factors (e.g., soil depth, soil properties, evaporation, and runoff) that can influence SM
changes due to drying and wetting processes (Albergel et al., 2008; Wagner et al., 1999).

2.3 Fully-Integrated Surface Water-Groundwater Model

The high-resolution fully integrated surface water-groundwater simulations are conducted using HydroGeoSphere (HGS)
140 (Aquanty, 2022, Hwang et al., 2014; Frey et al., 2021). HGS uses the one-dimensional (1D) Manning's open channel flow
equation to govern river/stream flow, the diffusion wave equation to govern two-dimensional (2D) overland flow, and the
Richards' equation to govern three-dimensional (3D) variably-saturated subsurface flow. The channel/surface/subsurface
regimes naturally interact with each other through the exchange of water fluxes in response to varying pressure gradients.
Unlike loosely or sequentially coupled groundwater-surface water models, HGS is a fully-integrated model, providing the
145 simultaneous solution of the channel, surface and subsurface flow regimes at each time step. Detailed information on HGS
can be found in the relevant documents (Aquanty, 2022, Hwang et al., 2014; Frey et al., 2021).

Within the model there are seven subsurface layers that are composed of 3D triangular prisms, formed by superimposing
eight mesh layers of planar elements from the soil surface downward to a depth of ~35 m. In total, there are 171,609 planar
150 elements per mesh layer, equating to a total 1,201,263 3D elements across the seven-layer subsurface domain. The 3D
unstructured finite element mesh that underpins the HGS model carries 125 m spatial resolution along Strahler 2+ streams
and rivers, and up to 375 m resolution in areas distal to the resolved surface water features. The 2D overland flow domain
(composed of planar elements) and the 1D channel domain (composed of linear elements) are both superimposed onto the
subsurface 3D domain. In the model subsurface domain, the three soil layers (0–25 cm, 25–50 cm, and 50–100 cm depths) of
155 3D elements were constructed by superimposing the four mesh layers of planar elements at the soil surface, 25 cm, 50 cm,
and 100 cm depths, respectively. The four mesh soil layers of planar elements can provide the simulated SM at the four
specific depths (soil surface, 25 cm, 50 cm, and 100 cm), while the three soil layers of 3D elements can provide the
simulated SM for the depth intervals of 0–25 cm, 25–50 cm, and 50–100 cm. The simulated SM from the planar element
mesh layer at the soil surface represents the simulated SSM. Underlying the three soil layers are the four hydrostratigraphic
160 layers (three Quaternary layers and one bedrock layer), with geometry and lithology derived from Logan et al. (2009). The
tile drains installed in the SNW (Fig. 1e) are not resolved in the model because of resolution constraints associated with the
size of the model domain and the necessity of carrying a practical number of finite elements. The influence of tile drainage
absence in the model will be discussed in this study (section 6.2).

165 Appropriate spin-up is essential for integrated surface-subsurface models (e.g., Ajami et al., 2014, 2015; Erdal et al., 2019).
Similar to Frey et al. (2021), the HGS model herein was initialized following a three-step procedure. Firstly, the model was



forced by long-term (~30-year) average annual net precipitation until steady-state groundwater heads and streamflow rates were established. Secondly, using steady-state as an initial condition, the model was forced by monthly normal liquid water flux and potential evapotranspiration for a decadal cycle, yielding a year over year dynamic equilibrium condition. Thirdly, using dynamic equilibrium as an initial condition, the model was forced with daily transient liquid water flux and potential evapotranspiration derived from Natural Resources Canada (NRCAN)'s gridded daily climate data sets (McKenney et al., 2011) in combination with snow water equivalent data derived from the ERA5 land surface reanalysis product (Muñoz-Sabater et al., 2021). The daily transient simulations extended from January 1, 2008 to December 31, 2017, and were run multiple times, with model performance only evaluated after the second set of simulations. The model calibration primarily involved manually tuning the soil hydraulic conductivity and the Manning's surface roughness coefficient for the 1D river/stream channels. The objective of calibration was to optimize surface water flow rates at the hydrometric stations (Fig. 1d) and groundwater levels at the monitoring wells (Fig. 1e). Subsequent analysis is based on the March 31, 2015 (the date when SMAP started operation) to December 31, 2017 time frame, using daily transient output data from the calibrated HGS model.

2.4 Comparison Analysis and Performance Metrics

2.4.1. Evaluation of SMAP and Modeled Soil Moisture

The SM estimates from the SMAP product and HGS model simulations are evaluated against the SM measurements from in situ monitoring sites (Fig. 1c). The specification of in situ SM measuring is provided in Table A1. Since the in situ SM sites are sparse, the evaluation is available only at point-scale. SMAP SSM and HGS simulated SSM estimates are evaluated using the 0–5 cm in situ SM measurements. The HGS simulated root zone SM is evaluated at two depth profiles: 0–25 cm (i.e., the simulated SM in the model's top soil layer against a depth-weighted average of in situ measurements in the top 25 cm soil) and 0–100 cm (i.e., a depth-weighted average of simulated SM from the model's three soil layers versus a depth-weighted average of in situ measurements in the top 100 cm soil). At each in situ site, the unbiased Root Mean Squared Error (ubRMSE) and Pearson correlation coefficient (R) are computed based upon the daily time series using the following equations:

$$ubRMSE = \sqrt{E[(\theta_s - E[\theta_s]) - (\theta_i - E[\theta_i])]^2} , \quad (3)$$

$$R = E[(\theta_s - E[\theta_s])(\theta_i - E[\theta_i])](\sigma_s \sigma_i)^{-1} , \quad (4)$$

where $E[\bullet]$ is the expectation operator. θ_s and θ_i indicate the daily time sequences of satellite (or model) soil moisture and in situ data, respectively. σ_s and σ_i denote the standard deviations of θ_s and θ_i , respectively.

195



2.4.2 Evaluation of HGS Simulated Streamflow and GW Level

The simulated streamflow rates and GW levels in the fully-integrated modeling framework are physically linked to SM and GW flow, and are hence also a reflection of water dynamics in the variably-saturated subsurface domain. The simulated streamflow is evaluated using streamflow measurements from Water Survey of Canada (WSC) hydrometric stream gauges (Fig. 1d), and performance is assessed with the Nash-Sutcliffe efficiency (NSE) in Eq. (5):

$$NSE = 1 - E[(Q_{obs} - Q_{sim})^2] / E[(Q_{obs} - E[Q_{obs}])^2], \quad (5)$$

where $E[\bullet]$ is the expectation operator. Q_{obs} and Q_{sim} indicate the daily time sequences of observed and simulated stream discharge values, respectively. NSE ranges from $-\infty$ to 1 with 1 as the optimal value.

The simulated GW levels are compared to GW level measurements provided by the Provincial Groundwater Monitoring Network (PGMN, <https://data.ontario.ca/dataset/provincial-groundwater-monitoring-network>) wells (Fig. 1e). Since the temporal variability information is of the most interest for the simulated GW levels in this study, the Pearson correlation coefficient (R) between the temporal variations of simulated and observed GW level anomalies is calculated at each GW monitoring well across the SNW. The GW level anomalies represent the departures from their respective average over the evaluation period (March 31, 2015 to December 31, 2017).

2.4.3 Comparison between SMAP and HGS Model Simulations

The SMAP data (SSM and SWI) are compared to the HGS model simulations (SSM, subsurface SM, and GW storage) to quantify the vertical coupling and response time differences between satellite SM and the variably-saturated subsurface water. The comparisons are made at both the 9-km (SMAP product grid) resolution and the entire watershed, and are measured using the unbiased Root Mean Squared Difference (ubRMSD), R , anomaly R , and Spearman's rank correlation (ρ), depending upon the variables under comparison. The ubRMSD and R are computed using the equations similar to Eq. (3) and Eq. (4), but with the two variables from the SMAP and HGS simulation, respectively. The anomaly R calculation is similar to the R calculation, but uses the anomaly time series of the variables, which are defined as departures of raw values from their monthly normals over the study period (2015–2017). For each variable, all three-year (2015 to 2017) monthly data must be valid for computing the monthly normal of a calendar month. The Spearman's rank correlation (ρ) is calculated as,

$$\rho = 1 - \frac{6 \sum d^2}{n(n^2-1)}, \quad (6)$$

where d represents the difference between the ranks of the SMAP and HGS model variables, and n denotes the length of data. In this study, ρ is used for time scale quantification for water transport from the surface soil layer to deeper unsaturated/saturated zones.



225 3 Evaluation of SMAP SSM and Model Simulations

The evaluation scores for the SMAP SSM and HGS SM across the individual in situ sites are listed in Table 1. In this study, the in situ SSM (0–5 cm) measurements are only available at Agriculture and Agri-Food Canada’s Ontario Real-Time In-Situ Soil Monitoring for Agriculture (RISMA) stations (Tabel A1). Fig. 2 shows the SSM time series from SMAP, HGS model, and in situ measurements at the four Ontario RISMA stations. Overall, both the SMAP and HGS modeling captured the in situ observed SSM temporal variability very well (Fig. 2). Both the SMAP SSM and simulated SSM showed a mean ubRMSE of about 0.05–0.06 m³ m⁻³ and a mean *R* of about 0.7 with the in situ measurements (Table 1). The performance of SMAP SSM over the SNW is very similar to that over the Great Lakes region (Xu, 2020; Xu and Frey, 2021), which is approximately adjacent to the study region SNW.

235 **Table 1** Soil moisture (SM) performance metrics

Metrics	Station ID	SMAP SSM	HGS SM		
			Near Surface	0–25 cm	0–100 cm
	RISMA ON2	0.056	0.050	0.038	0.021
	RISMA ON4	0.047	0.061	0.047	0.028
	RISMA ON5	0.055	0.041	0.042	0.022
	RISMA ON6	0.079	0.066	0.040	0.030
ubRMSE (m ³ m ⁻³)	Metcalf	—	—	0.053	—
	Pleasant Valley	—	—	0.024	0.013
	WEBs@11-14	—	—	—	0.023
	WEBs@20	—	—	—	0.035
	Winchester	—	—	0.033	—
	Average	0.059	0.054	0.040	0.025
<i>R</i>	RISMA ON2	0.67	0.76	0.74	0.76
	RISMA ON4	0.72	0.56	0.67	0.73
	RISMA ON5	0.66	0.82	0.75	0.86
	RISMA ON6	0.71	0.80	0.82	0.76
	Metcalf	—	—	0.70	—
	Pleasant Valley	—	—	0.81	0.77
	WEBs@11-14	—	—	—	0.88
	WEBs@20	—	—	—	0.70
	Winchester	—	—	0.77	—
Average	0.69	0.74	0.75	0.78	

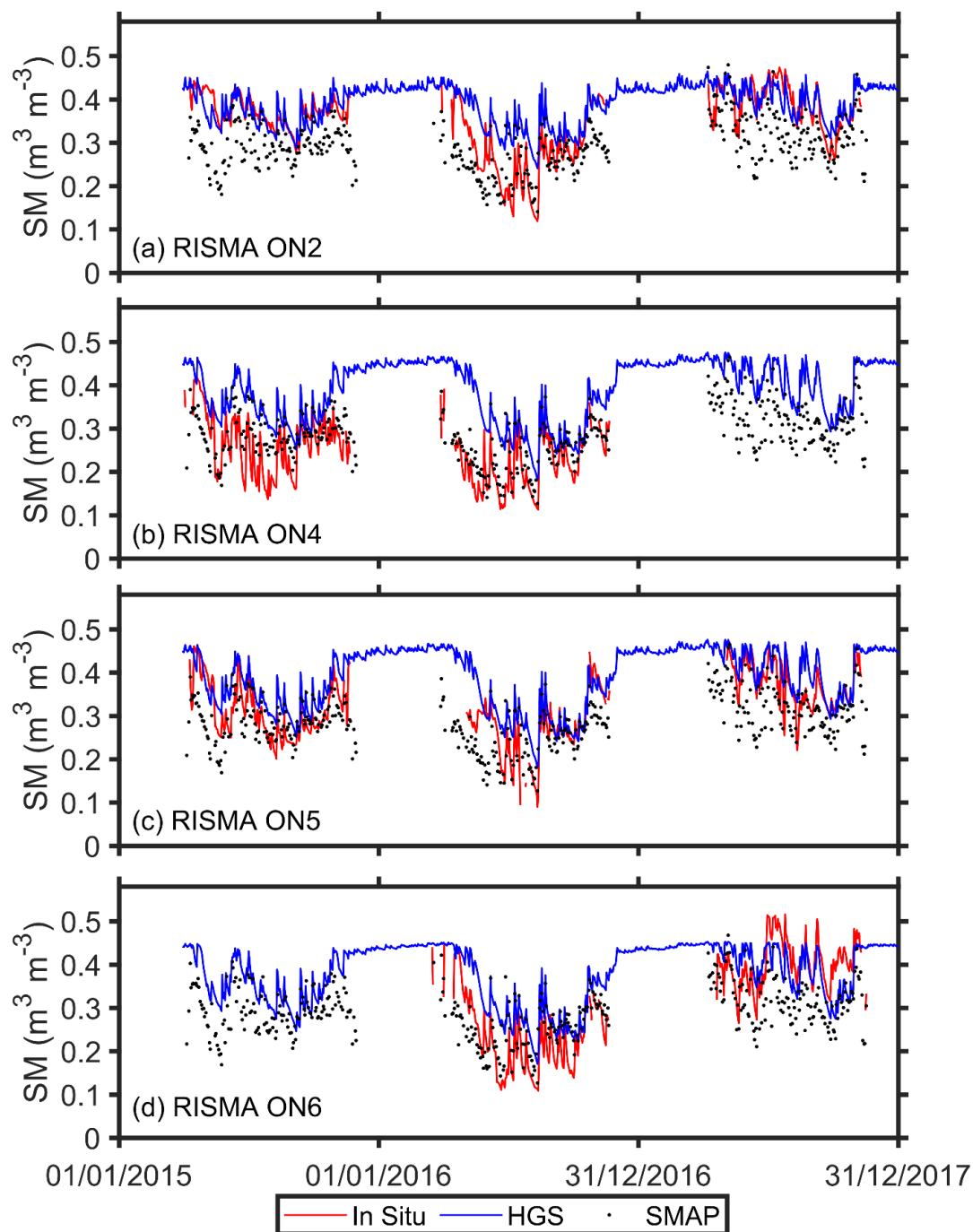


Figure 2: The SSM time series from SMAP, HGS model simulation, and in situ measurements, respectively, at the four RISMA stations: (a) ON2, (b) ON4, (c) ON5, and (d) ON6.



240

Figs. A1 and A2 show the root zone SM time series comparison between HGS simulations and in situ measurements for the 0-25 cm and 0-100 cm soil layers, respectively. Overall, the HGS simulations agree with the in situ measurements very well in terms of the SM temporal variability in the two soil profiles across all available validation sites (Figs. A1 and A2), with the mean R close to or exceeding 0.75 for both soil profiles (Table 1). Unsurprisingly, the ubRMSE for the HGS soil moisture decreases with the increasing soil depth (Table 1), resulting from a smaller soil moisture temporal variability in a deeper profile (e.g., Albergel et al., 2008; Xu, 2020).

Fig. A3 presents the simulated and observed hydrographs along with the calculated NSE values at the seven WSC streamflow gauges across the study watershed (as shown in Fig. 1d). The HGS simulations performed well in capturing the timing of peak flows. The NSE values are typically high, exceeding 0.62 for all gauges, although the underestimation of peak flows is also evident in the HGS hydrographs. A possible explanation for the flow underestimation is that the tile drain flow, which was not resolved in the present HGS model simulations, is also a source of discharge for streams (due to a shallow water table) in the real-world SNW. Further, the comparisons between the simulated and observed GW level anomalies at the eight GW monitoring wells were provided in Fig. A4. In general, the GW temporal variability was well reproduced by the HGS modelling across the monitoring wells, with R ranging from 0.4 to 0.86.

Overall, the SMAP SM product can capture the SSM variability well over the study region, while the HGS simulations match the observed surface/subsurface water dynamics well. This supports the HGS model's application towards quantifying the dynamic behavior of surface/subsurface hydrologic conditions, and to testing linkages between SMAP measurements and simulated water content in the variably saturated subsurface.

4. Comparisons between SMAP SSM and HGS Model Simulations

4.1 Comparison at the 9-km Scale

In this section, we compare the SMAP SSM with the HGS simulated SM at the SMAP product grid (9-km) scale. Since the HGS model has a higher resolution than the 9-km SMAP grid (see section 2.3), the model SM estimates are spatially aggregated (i.e., averaged) within each SMAP grid cell. Fig. 3a illustrates the ubRMSD values across all SMAP grids for the SMAP SSM and HGS SSM comparison, with the summarized ubRMSD provided in Fig. 4a. The SMAP grid-scale ubRMSD values range from 0.04 to 0.06 $\text{m}^3 \text{m}^{-3}$ and are typically lower in the forested areas than over the agricultural fields (Fig. 3a with the land cover map provided in Fig. 1b). The average ubRMSD between the SMAP and HGS SSM estimates is about 0.047 $\text{m}^3 \text{m}^{-3}$ at the 9-km scale (Fig. 4a).

270

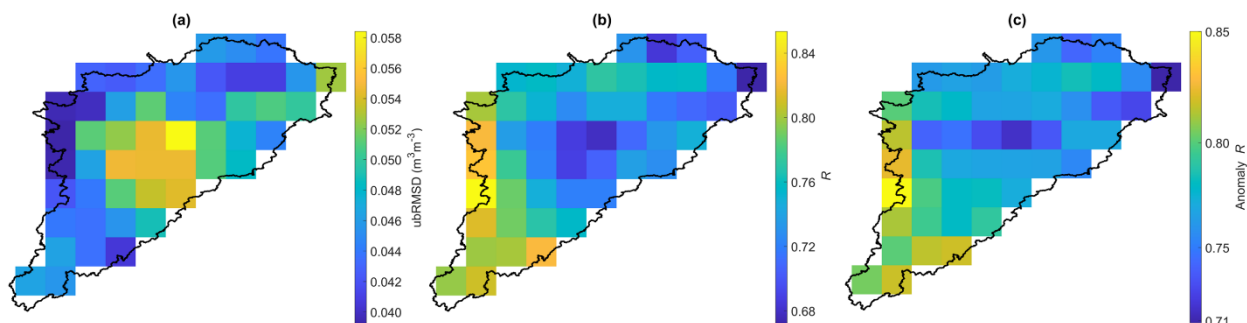
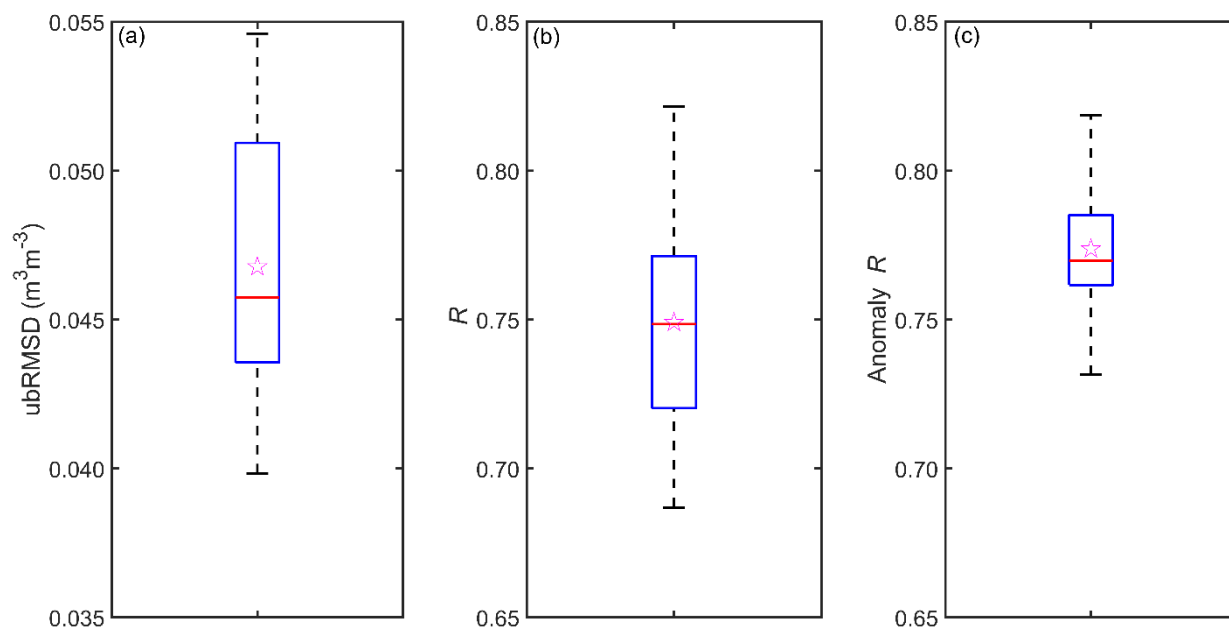


Figure 3: (a) ubRMSD, (b) R , and (c) anomaly R between the SMAP SSM and HGS SSM across all SMAP grids.



275 **Figure 4:** Boxplots of (a) ubRMSD, (b) R , and (c) anomaly R between the SMAP SSM and HGS SSM, summarized from all 9-km grids within the study watershed. In each box, the red line and the star denote the median and mean of the sample data, respectively; the lower and upper edges of the box indicate the 25th and 75th percentiles, respectively; and the bottom and top ends of the whiskers denote the 5th and 95th percentiles, respectively.

280 Fig. 3b shows the R values between the SMAP SSM and the HGS simulated SSM across all individual SMAP grids, which are summarized using the boxplot in Fig. 4b. The simulated SSM can capture the SMAP observed SSM dynamics quite well at the 9-km grid scale with an average R exceeding 0.7 (Fig. 4b). In terms of the spatial variability, the R values are typically higher over the forests than their counterparts over the agricultural lands (Fig. 3b), which may be in part due to tile drainage not fully captured by the model (see section 6.2). The anomaly R results (Figs. 3c and 4c) are similar to the R results,
285 indicating that the obtained correlations between SMAP and the HGS model are dominated by the day-to-day variations

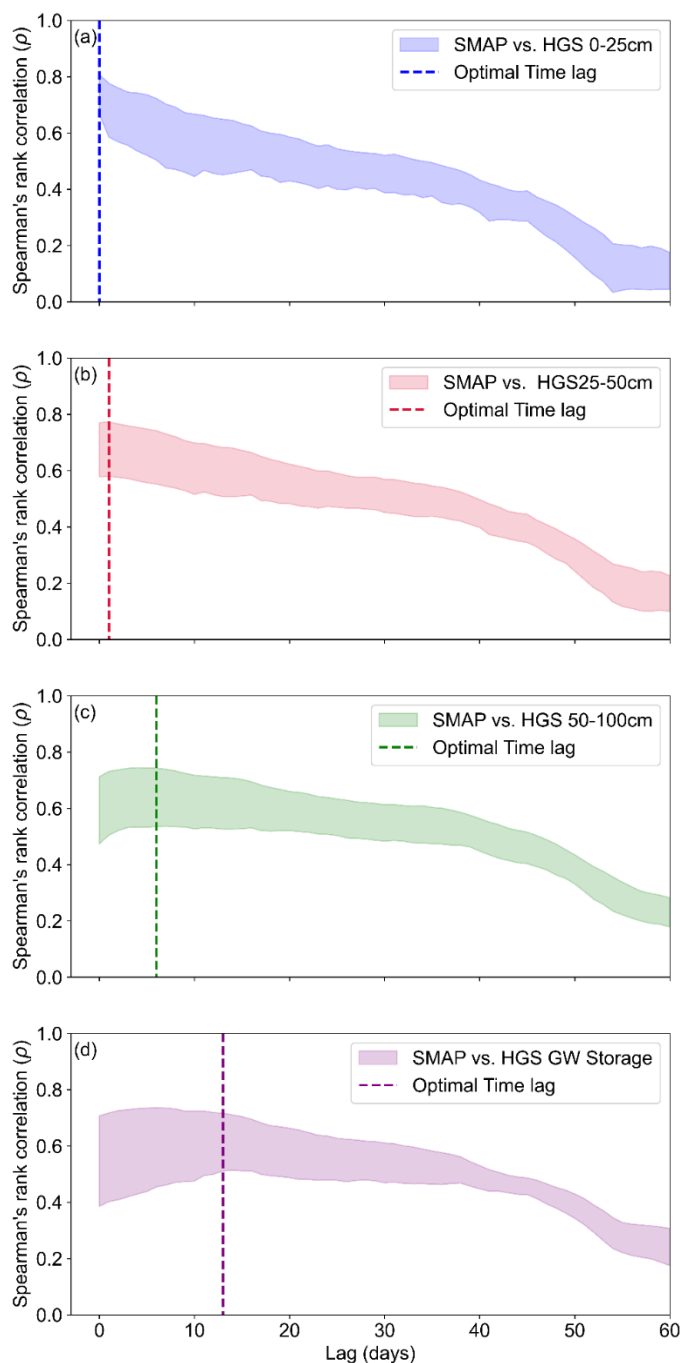


(rather than the seasonal trends) in the SM time series. Further, the linear regression between SMAP SSM (independent variable) and HGS SSM (dependent variable) suggests that modeled SSM is systematically wetter than SMAP SSM (intercept > 0) but shows a smaller change in response to every unit change in SMAP SSM (slope < 1) across the watershed (Figs. A5 and A6).

290

To examine the linkage between SMAP SSM and water storage variability in the deeper subsurface, time lagged cross-correlations between the SMAP SSM and simulated subsurface SM and GW storage were calculated for each 9-km grid. Here the Spearman's rank correlation (rather than the Pearson correlation) is used for the time lagged cross-correlation analysis since the monotonic (rather than linear) relationship is of the most interest for identifying the phase difference between near-surface and deeper subsurface water content variability. Fig. 5 presents the Spearman's rank correlations (the 5th to 95th percentiles from all SMAP grids over the study watershed) between the time series of SMAP SSM and the HGS simulated subsurface SM (0–25 cm, 25–50 cm, and 50–100 cm depths) and GW storage for time lag ranging from 0 to 60 days. The optimal time lags (in days) and corresponding highest Spearman's rank correlations across all SMAP grids are provided in Figs. A7 and A8, respectively.

300



305 **Figure 5:** Spearman's rank correlation coefficients between the time series of SMAP SSM and HGS simulated SM from (a) 0–25 cm depth, (b) 25–50 cm depth, and (c) 50–100 cm depth, respectively, as well as (d) GW storage for time lags ranging from 0 to 60 days. Positive lags indicate that the SMAP data are leading the HGS simulations. In each plot, the shaded band represents the 5th to 95th percentiles of the results from all SMAP grids within the study watershed. For each SMAP grid, the optimal time lag is defined as the one with the maximum Spearman's rank correlation between SMAP SSM and HGS simulated variable. The vertical dashed line indicates the median of the optimal time lags from all SMAP grids.



Unsurprisingly, the simulated SM in the 0–25 cm depth (Figs. 5a and A7a) showed simultaneous response (a time lag of 0
310 day) to the SSM variability captured by SMAP across the study watershed. By contrast, simulated water content variations in
the deeper subsurface showed a delayed response relative to the SMAP SSM variability. The optimal time lag increased with
depth, with a median delay of about 1–2 days for the 25–50 cm SM (Fig. 5b), about 6 days for the 50–100 cm SM (Fig. 5c),
and about 11–12 days for the GW storage (Fig. 5d).

315 By comparing the spatial distribution of time lags on a SMAP grid cell basis (Fig. A7) to the soil distribution (Fig. 1c), the
time delay for deeper zones is typically shorter in regions with well drained soils (e.g., the southwestern portion of SNW)
than in areas with poorly or imperfectly drained soils (e.g., the northern SNW), reasonably reflecting the impact of soil
properties on deeper subsurface hydrologic response. It should also be noted that the quantified time delay in deep
subsurface water dynamics did not explicitly account for the impact of tile drainage due to the absence of tile drains in the
320 model. The maximum correlations (corresponding to the optimal time lags) between the SMAP SSM and simulated
subsurface water also showed a clear spatial pattern, with higher values in the southwestern SNW (Fig. A8), which
corresponds to the regions with well drained soil (Grenville and Farmington soils in Fig. 1c). Overall, the soil texture
showed an important impact on the vertical coupling length (correlations) and response time differences between satellite
SSM and the variably-saturated subsurface water.

325 **4.2 Comparison at the Watershed Scale**

Fig. 6 compares the SMAP and HGS simulated time series for the watershed-averaged SSM. Although the simulated SSM is
systematically wetter than SMAP SSM, the simulated results match the SMAP measurements very well in terms of SSM
variations, with both the R and anomaly R between them exceeding 0.8 and an ubRMSD less than $0.04 \text{ m}^3 \text{ m}^{-3}$. The observed
mean biases between the SMAP and modelled SSM may in part be related to the calibration of the SMAP SM retrieval
330 algorithm. Although the SMAP SM retrievals can capture the SSM variability very well, they typically show an
underestimation of SSM (i.e., drier surface soils) over Canadian agricultural regions due to issues with correcting the effects
of growing vegetation (e.g., Colliander et al., 2017). In addition, the absence of tile drainage in the HGS model could cause
a wet bias over the tile drained landscape (~25% of the entire watershed) and therefore moderately increase the wetness of
the simulated watershed-averaged SSM. Given the scarcity of in situ SM measurements, this study is unable to investigate
335 whether the SMAP retrieval algorithm or the modeling should be blamed for the bias. However, such bias has a negligible
effect on this study since the SM temporal variations from the SMAP and HGS model are of primary interest herein.

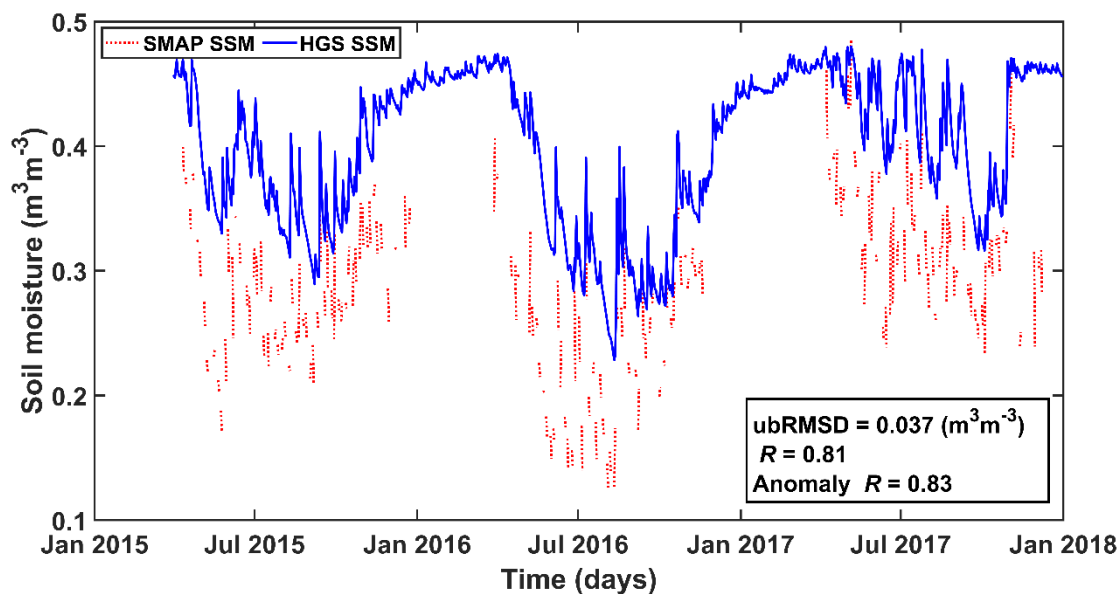


Figure 6: Comparison between the SMAP and HGS simulations for the watershed averaged SSM time series.

340 The relationships between variations of SMAP SSM and HGS simulated water content in deeper unsaturated/saturated zones at the watershed scale are quantified in Fig. 7. Fig. 7a shows the time series of the simulated watershed-averaged SM in the 0–25 cm, 25–50 cm, and 50–100 cm depths and watershed integrated GW storage, in comparison with the watershed-averaged SMAP SSM. The Spearman’s rank correlations between the SMAP SSM and the HGS simulated subsurface water for time lags ranging from 0 to 60 days are provided in Fig. 7b. Variations in simulated subsurface water are highly
345 correlated across the different depth intervals. The surface soil layer (0–25 cm) is directly impacted by influxes and effluxes of water and therefore shows the largest day-to-day water content variability, while the 50–100 cm SM and GW storage show comparably smoother day-to-day fluctuations (Fig. 7a). Accordingly, in Fig. 7b, variations in time-lagged correlation between SMAP SSM and simulated subsurface water become smoother as the subsurface depth increases, which also reflects the gradual filtering of high-frequency signals in subsurface water content with the increasing depth.

350

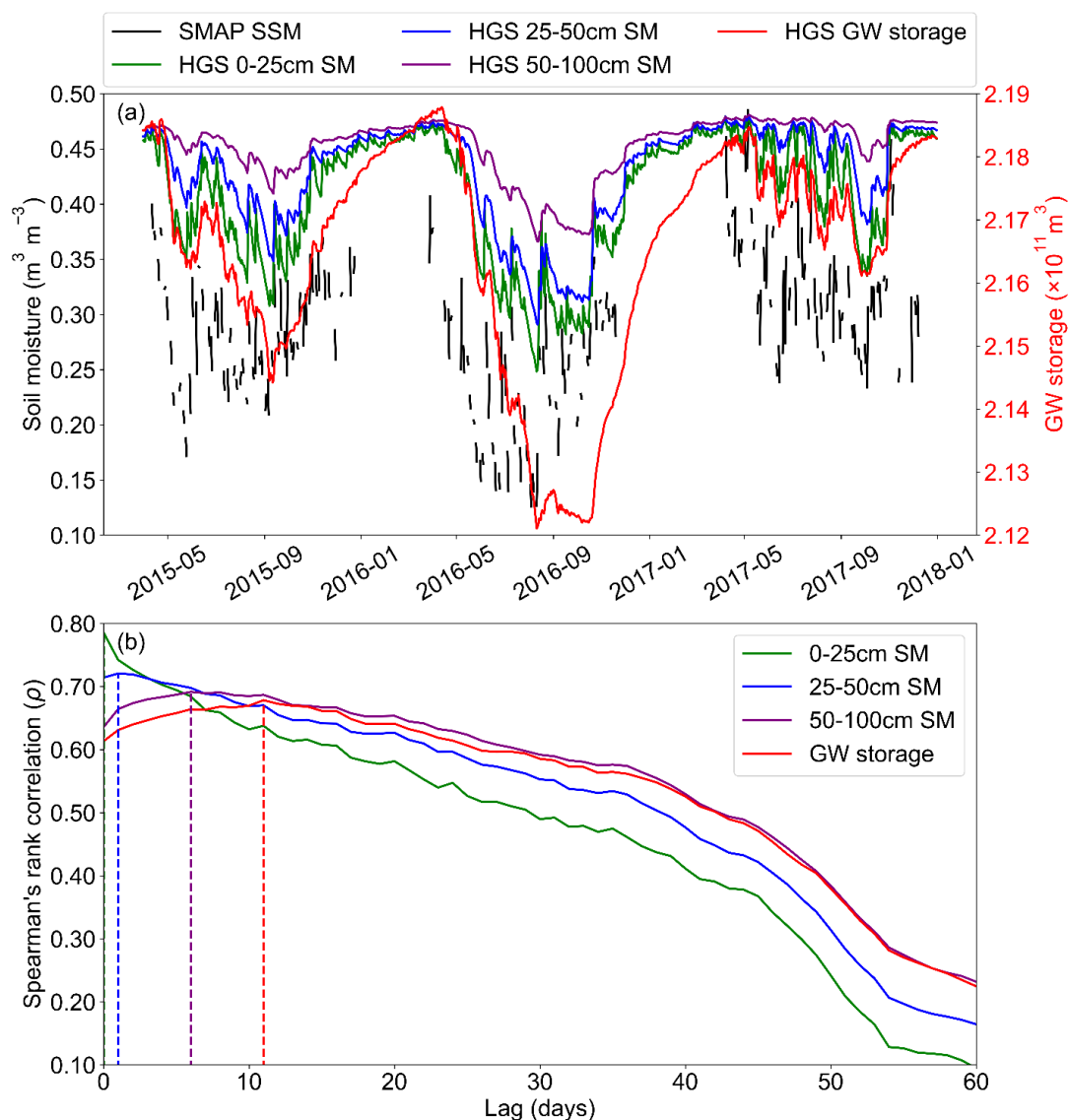


Figure 7: (a) Daily time series of HGS simulated watershed-averaged SM in the 0–25 cm, 25–50 cm, and 50–100 cm depths, and watershed integrated GW storage, along with watershed-averaged SMAP SSM. (b) Spearman’s rank correlation between the watershed-averaged SMAP SSM versus the HGS simulated watershed-averaged 0–25 cm SM, 25–50 cm SM, 50–100 cm SM, and watershed integrated GW storage, respectively, for time lag ranging from 0 to 60 days. Positive lags indicate that SMAP data lead the HGS simulations. In (b), for each pair of comparisons, a vertical dashed line is provided to indicate the location of the optimal time lag corresponding to the maximum Spearman’s rank correlation.

A very good agreement is observed between the variations of the watershed-averaged SMAP SSM and HGS simulated watershed-averaged surface layer (0–25 cm) SM with their highest Spearman’s rank correlation coefficient reaching around 0.8, which occurring at a time lag of 0 day (i.e., the delay is less than 1 day and cannot be resolved at daily time steps). With

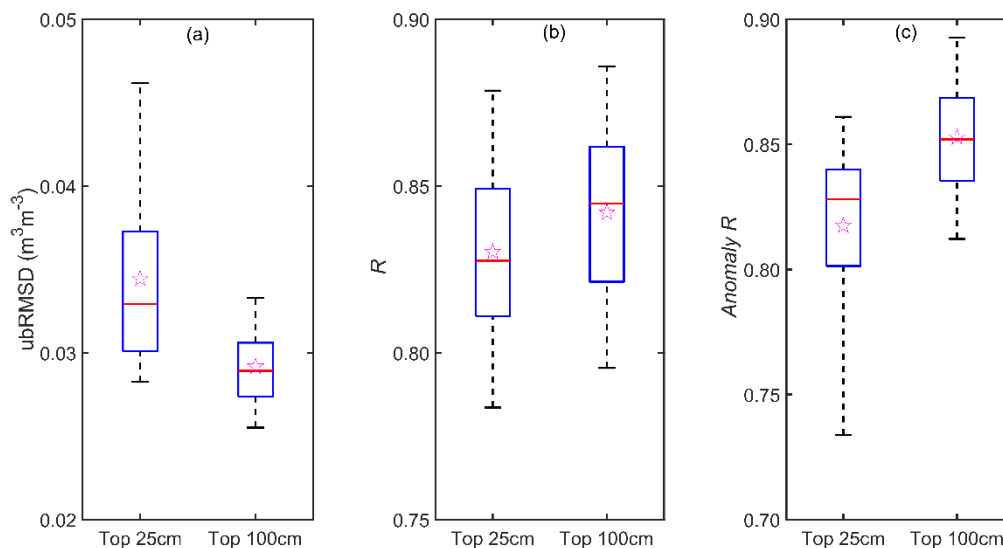


the time lag increasing, the correlation between SMAP SSM and the simulated 0–25 cm SM drops rapidly (green in Fig. 7b). The variations of deeper subsurface SM and GW storage are also in relation to the SMAP SSM variability, but showing a delayed response. At the watershed scale, the 25–50 cm SM, 50–100 cm SM and GW storage showed the highest Spearman's rank correlation with the SMAP SSM variability at a temporal delay of ~1 day, ~6 days, and ~11 days, respectively (Fig. 7b), which is very similar to the analysis at the 9-km scale (Fig. 5).

5. Comparisons Between SMAP-Derived SWI and HGS Model Simulations

5.1 SMAP SWI estimation based upon classic time length T

Linkage between SMAP SSM-derived SWI and HGS simulations is investigated here. Firstly, SWI based upon the model-independent characteristic time length T (so that the calculated SWI is entirely independent of the model simulations) is compared to simulated subsurface SM. It must be acknowledged that ideally, the time length T (model-independent) should be estimated using in situ SM measurements (e.g., Wagner et al., 1999, Tian et al., 2020). However, given the scarcity of in situ SM data and the relatively large spatial scale of the analysis herein, it is not possible to determine the time length T (model-independent) based upon evaluation with in situ data. To this end, $T = 15$ days and $T = 20$ days (taken from Wagner et al., 1999), which represent the classic T values for SWI estimation in the surface soil layer (0–20 cm) and the root zone soil layer (0–100 cm), respectively, were used for calculating the model-independent SWI across the 9-km grids. The calculated SWI using $T = 15$ days are compared to the HGS 0–25 cm SM, while the calculated SWI using $T = 20$ days are compared to the HGS 0–100 cm SM. Fig. A9 presents the ubRMSD, R , and anomaly R between SWI and HGS simulated subsurface SM across all 9 km grids. The 9 km grid-scale evaluation metrics are summarized in Fig. 8. Across the SNW, the 9-km scale ubRMSD between SWI and HGS SM typically ranges from 0.03 to 0.05 $\text{m}^3 \text{m}^{-3}$ (with an average of 0.035 $\text{m}^3 \text{m}^{-3}$) for the top 25 cm layer (Figs. 8a and A9a) and less than 0.04 $\text{m}^3 \text{m}^{-3}$ (with an average of about 0.03 $\text{m}^3 \text{m}^{-3}$) for the top 100 cm layer (Figs. 8a and A9b). In the two soil depths (top 25 cm and top 100 cm), both the R and anomaly R between SWI and HGS SM are very high and typically exceed 0.70 (Figs. A9c-f), with their means exceeding 0.82 (Figs. 8b and 8c).



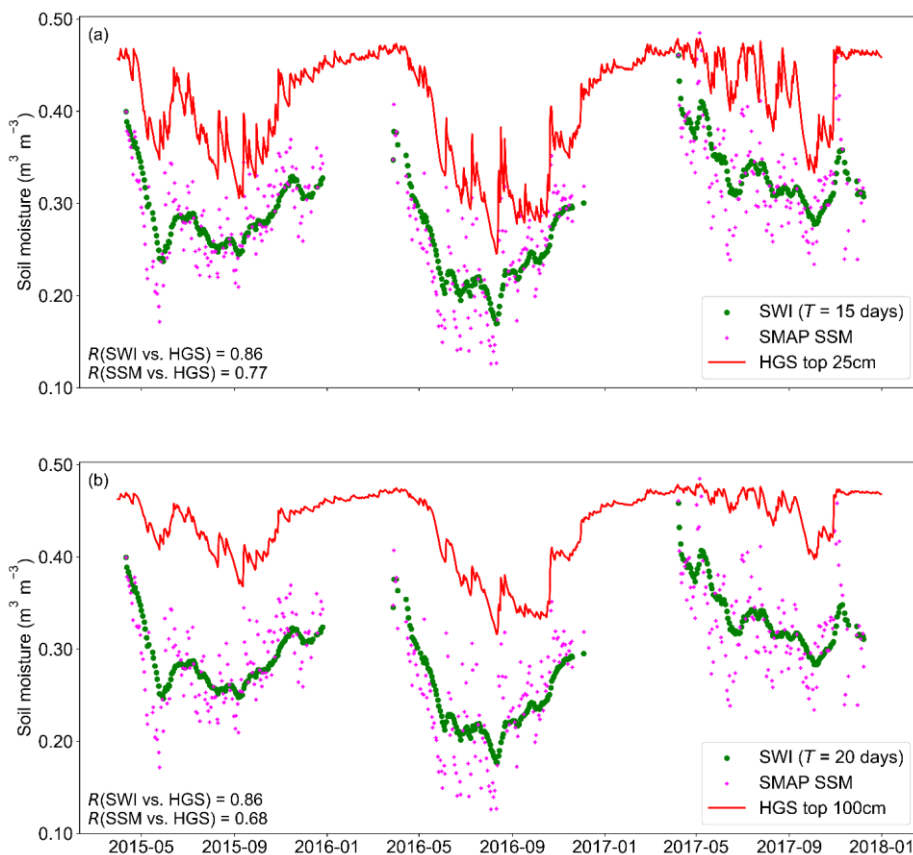
385

Figure 8: (a) Boxplots for the ubRMSD between the SMAP SSM-derived SWI (using $T = 15$ days) and HGS simulated top 25 cm SM and the ubRMSD between the SMAP SSM-derived SWI (using $T = 20$ days) and HGS simulated top 100 cm SM, respectively, summarized from all SMAP 9-km grids over the study watershed. In each box, the red line and the star denote the median and mean of the sample data, respectively; the lower and upper edges of the box indicate the 25th and 75th percentiles, respectively; and the bottom and top ends of the whiskers denote the 5th and 95th percentiles, respectively. (b) and (c): Similar to (a), but for the correlation coefficient R and anomaly R , respectively.

390

Further, the SWI time series are calculated from the watershed averaged SMAP SSM series (using $T = 15$ days and $T = 20$ days, respectively) and are then compared with the watershed averaged HGS SM (top 25 cm and top 100 cm, respectively) (Fig. 9). The SWI time series represent the simulated SM variability in the two soil layers very well, with an R value close to 0.9. Unsurprisingly, for both soil depth intervals (top 25 cm and top 100 cm), the simulated SM showed a higher correlation with the SWI than with the SMAP SSM (Fig. 9).

395



400 **Figure 9:** (a) Watershed-scale time series of SMAP SSM, SMAP SSM-derived SWI (using $T=15$ days), and HGS simulated top 25 cm SM. (b) Watershed-scale time series of SMAP SSM, SMAP SSM-derived SWI (using $T=20$ days), and HGS simulated top 100 cm SM. In each plot, the correlation R between SWI (or SMAP SSM) and simulated SM is provided.

Fig. 10 presents the comparison of variations in the HGS simulated watershed integrated GW storage and the watershed
405 scale SWI in the 0-100 cm soil (using $T=20$ days). The SWI and GW storage share very similar temporal variations, with their best correlation occurring at a time lag of about 2 days. This may demonstrate the potential of SWI to predict the day-to-day variations in GW.

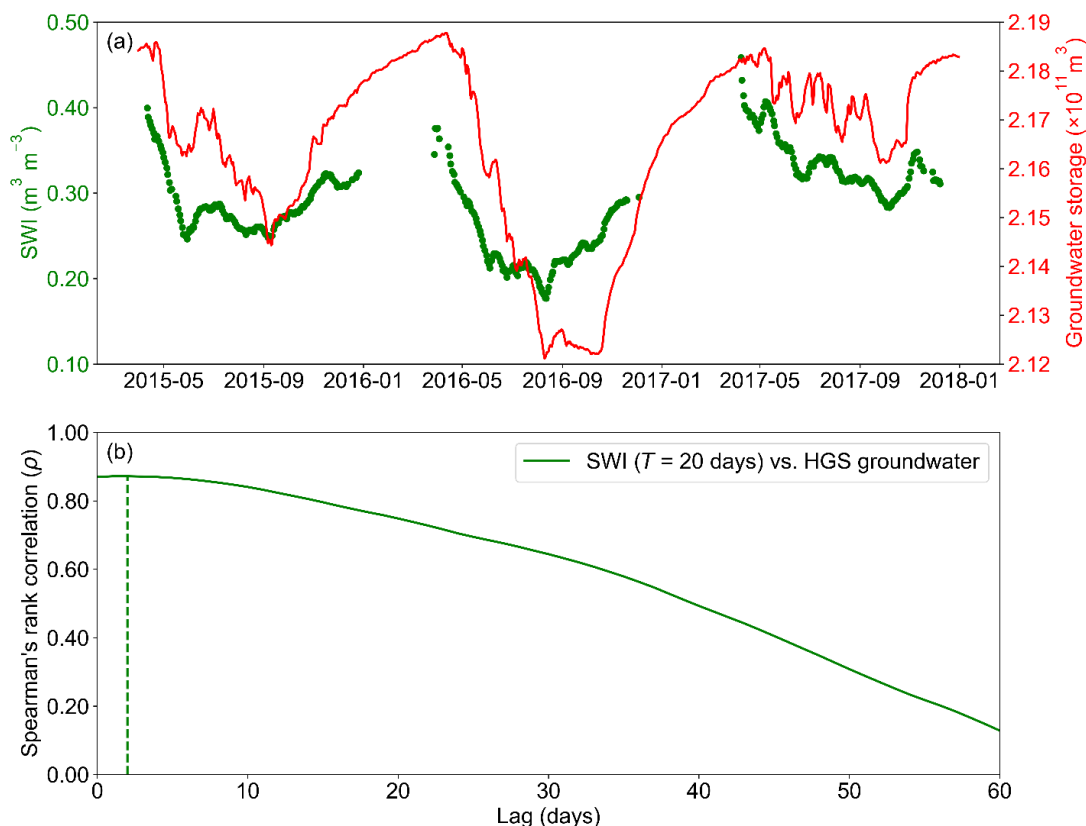


Figure 10: (a) Daily spaced time series of watershed-scale SWI (using $T=20$ days) and HGS simulated watershed integrated GW storage. (b) Spearman's rank correlations between the two time series in (a) for time lag ranging from 0 to 60 days. Positive lags indicate that the SWI leads the GW. In (b), the vertical dashed line indicates the location of the time lag leading to the maximum Spearman's rank correlation between the two series.

5.2 Identification of Optimal Characteristic Time Length T_{opt}

Although the optimal characteristic time length T_{opt} for SWI estimation has been investigated for many regions across the world (e.g. Bouaziz et al., 2020; Ceballos et al., 2005; Tian et al., 2020; Wagner et al., 1999; Zhang et al., 2017), Canadian agricultural watersheds are typically underrepresented in this regard. In this part, T_{opt} is identified for the study watershed by optimally matching variations in SWI and HGS simulated subsurface SM. First, at each SMAP grid, SWI is calculated from the SMAP SSM series for the characteristic time length T varying between 1 and 100 days. Then, Spearman's rank correlations between the SMAP-derived SWI for each value of T and the HGS simulated subsurface SM (from three depth intervals: 0–25 cm, 0–50 cm, and 0–100 cm) are calculated. For each depth interval, the T value corresponding to the highest Spearman's rank correlation is defined as the optimal T_{opt} . The optimal T_{opt} (in days) and the associated highest Spearman's rank correlations across all SMAP 9-km grids are provided in Fig. A10. A comparison between Fig. A10 and the soil map



(Fig. 1c) indicates that the spatial variability of T_{opt} is impacted by the soil texture. T_{opt} is typically longer for the landscape with poorly (e.g., Bearbrook) or imperfectly (e.g., Achigan) drained soils than for regions with well drained soils (e.g., Farmington).

The frequency distribution of T_{opt} at the 9-km grid scale is provided in Fig. A11, while Fig. 11a presents the Spearman's rank correlations (the 5th to 95th percentiles from all SMAP grids over the study watershed) between the HGS simulated SM (0–25 cm, 0–50 cm, and 0–100 cm depths, respectively) and the SWI using T from 1 to 100 days. Across the SNW, the 9-km grid scale T_{opt} ranges largely from 14 to 26 days (Fig. A11a) with a median of 21 days (Fig. 11a) for the 0–25 cm layer, from 20 to 32 days (Fig. A11b) with a median of 24 days (Fig. 11a) for the 0–50 cm layer, and from 26 to 43 days for the 0–100 cm (Fig. A11c) with a median of 31 days (Fig. 11a) for the 0–100 cm layer. On average, T_{opt} increases with the depth in the soil profile, which agrees with previous studies (e.g., Wagner et al., 1999, Tian et al., 2020; Zhang et al., 2017).

435

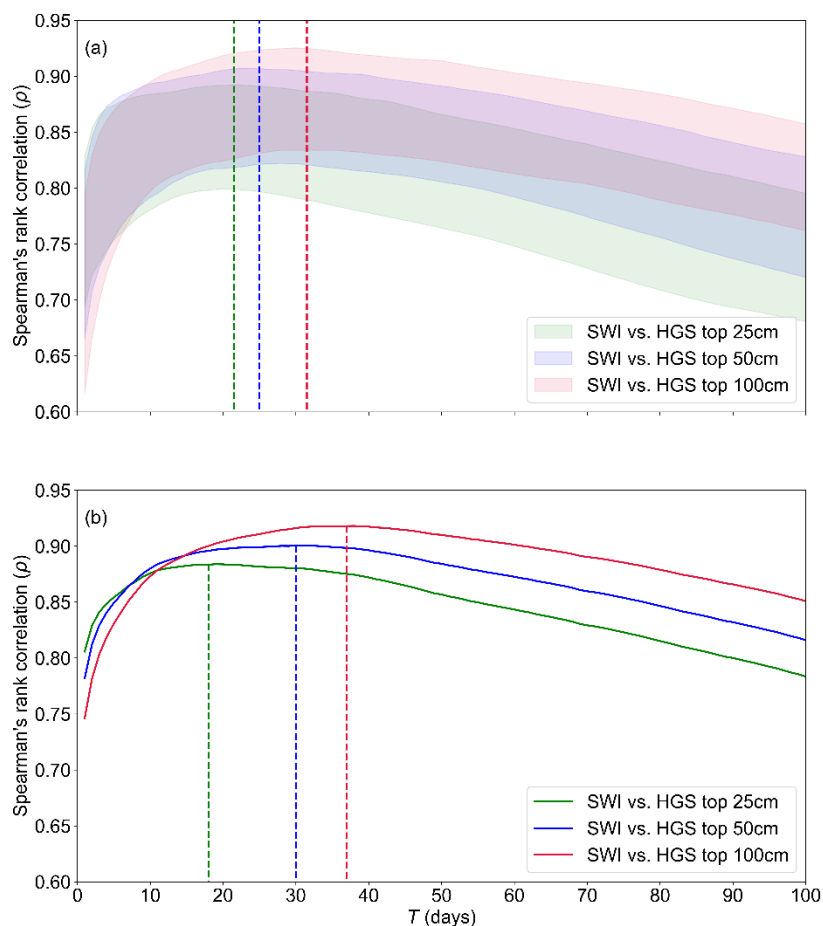


Figure 11: (a) Spearman's rank correlations coefficients between the time series (9-km grid scale) of HGS simulated SM (from the 0–25 cm, 0–50 cm, and 0–100 cm layers, respectively) and SMAP SSM-derived SWI for the characteristic time length T ranging from 1 to 100



440 days. For each layer, the shaded band represents the 5th to 95th percentiles of the results from all SMAP grids within the study watershed with a vertical dashed line indicating the location of the optimal T_{opt} median from all SMAP grids. (b) Spearman's rank correlation coefficients between the time series (watershed scale) of HGS simulated SM (from the 0–25 cm, 0–50 cm, and 0–100 cm layers, respectively) and SMAP SSM-derived SWI for T ranging from 1 to 100 days. For each layer, the vertical dashed line indicates the location of T_{opt} at the watershed scale.

445 The maximum Spearman's rank correlations between SWI and simulated subsurface SM (0–25 cm, 0–50 cm, and 0–100 cm layer) typically exceed 0.8 at the 9-km scale (Figs. A10b,d, and f). By comparing Fig. A10 and the land cover map (Fig. 1b), the forested area typically shows higher maximum Spearman's rank correlations between the SWI and simulated subsurface SM than the agricultural fields, which again can be at least partially related to the absence of discretely resolved agricultural tile drainage in the model (see section 6.2).

450 Fig. 11b provides Spearman's rank correlations between watershed averaged HGS subsurface SM and the SWI estimated from watershed averaged SMAP SSM for T varying from 1 to 100 days. The watershed-scale T_{opt} is about 19 days, 30 days, and 38 days for the 0–25 cm, 0–50 cm, and 0–100 cm layers, respectively, showing a clear increase of T_{opt} with increased soil depth (Fig. 11b). Across the three layers, the watershed-scale T_{opt} falls within the range of the most frequently occurring
455 T_{opt} at the 9-km scale (14 to 26 days for the 0–25 cm layer, 20 to 32 days for the 0–50 cm layer, and 26 to 43 days for the 0–100 cm layer as indicated in Fig. A11), indicating no significant change in T_{opt} across the two spatial scales.

In addition, note that at both spatial scales and across the three layers, the correlations between the calculated SWI and modeled SM are very strong for a range of T values surrounding T_{opt} . For example, the simulated 0–100 cm SM shows a
460 correlation > 0.9 with SWI for T ranging from 19 to 60 days at the watershed scale (Fig. 11b), while a correlation > 0.8 can be obtained between the simulated 0–100 cm SM and SWI for T ranging from 12 to 68 days at the 9-km scale (Fig. 11a). The selected model-independent value of $T = 20$ days for the 0–100 cm layer SWI (section 5.1) falls within both T ranges and is therefore suitable for the 0–100 cm SWI estimation at both spatial scales (Figs. 8 and 9). Similarly, the selected model-independent value of $T = 15$ days for the 0–25 cm layer SWI is also suitable for both spatial scales.

465 6. Discussion

6.1 Novelty and Improved Understanding of Near Surface–Subsurface Water Interaction

The novelty and advances provided by the study herein are as follows. Firstly, there is growing recognition that high resolution integrated surface water-soil moisture-groundwater modelling and forecasting is crucial for landscape scale water resource management (e.g., Simmons et al., 2020 and references therein). However, the assessment of large (i.e., watershed
470 to river basin) scale, high resolution integrated hydrologic simulations is often difficult due to a lack of spatially distributed observational information. This study attempts to fill this gap by presenting state-of-the-art satellite (SMAP) SM products as



a tool for evaluating integrated hydrologic simulations. The investigation indicates that the SMAP product and the fully-integrated hydrologic model simulations are matched very well in terms of the near surface (top few centimeters) SM variability at both the 9-km scale and the watershed scale. Further, the simulated deeper subsurface SM and GW storage fluctuation is lagged and smoothed in relation to the SSM variability captured by SMAP. The quantified connections between satellite measurements and modelling results demonstrate the capability of the fully-integrated hydrologic model to reproduce water content in the variably-saturated subsurface domain at a spatial scale that aligns with SMAP cell size. The application of SMAP towards high-resolution fully-integrated surface water-groundwater simulations expands upon previous inter-comparisons of satellite SM and simulations produced by land surface models (e.g., Al-Yaari et al., 2014; Dorigo et al., 2010; Draper et al. 2013; Parrens et al., 2012) or lumped models (e.g., Bouaziz et al., 2020).

Secondly, the study of coupling between near surface-subsurface water fluctuations was extended to the saturated zone (GW) and investigated at multiple spatial scales in this work. In previous work, vertical coupling analyses typically included only the unsaturated zone (surface SM versus root zone SM) for point-scale or small catchments. For example, Mahmood and Hubbard (2007) and Mahmood et al. (2012) quantified the coupling and time lags between near-surface and root zone SM dynamics at the point or field scale in the US state of Nebraska and suggested that the strength of the coupling was subject to soil type, land use type, and climate, with the temporal delay ranging from several days to a few months. Herein, the high-resolution integrated model simulations enabled an investigation on the vertical coupling and response time differences between dynamics of satellite SM and subsurface water in both unsaturated and saturated zones (i.e., variably-saturated subsurface water) at both the 9-km grid scale and the watershed scale. Results from the two spatial scales showed consistent variation in vertical coupling and response time across different layers. At both scales, root zone SM and GW fluctuation can be approximated by shifting the SMAP SSM time sequences forward by a soil property dependent optimal time length that increases with subsurface depth. Over the SNW, where poorly or imperfectly drained soils dominate the agricultural regions, the optimal time lag (relative to the SSM variability) is about 1 day for the 25–50 cm SM, about 6 days for the 50–100 cm SM, and about 11 days for the GW storage at both scales. These findings have important implications for exploiting the potential of SMAP (or other satellite) SSM measurements for estimating subsurface water dynamics in deeper unsaturated and saturated zones. In particular, large-scale satellite SSM monitoring could provide a quick approach for predicting deeper subsurface water storage changes at continental or global scales and alleviate the need for hydrologic modeling in some types of investigations.

Thirdly, this work suggests optimal and appropriate time length T values for satellite-based SWI estimation, and provides insight on linkages between SWI and subsurface water variability in both unsaturated and saturated zones over a representative Canadian agricultural watershed. Since T_{opt} for SWI estimation is dependent on a number of factors, including subsurface depth of interest, soil properties (e.g., Ceballos et al., 2005; de Lange et al., 2008; Wang et al., 2017), climate (e.g., Albergel et al., 2008; Mahmood et al., 2012; Wang et al., 2017), and land cover/land use (Bouaziz et al., 2020;



Mahmood and Hubbard, 2007), characterization of T_{opt} has been extensively studied. As pioneer of the SWI approach, Wagner et al. (1999) recommended a T_{opt} of 15 days and 20 days for the top 20 cm layer and top 100 cm layer, respectively, based on satellite and in situ SM monitoring over Ukraine. Zhang et al. (2017) reported a T_{opt} of 8 days for the 25 cm depth and 49 days for the 75 cm depth based upon in situ measurements in the US state of Oklahoma. Bouaziz et al. (2020) indicated that T_{opt} values varied significantly across different regions; and when using the SMAP SPL3SMP-E SM product (also used in the present study), T_{opt} values ranged from ~ 2 to 42 days (within the 5% to 95% percentiles) with a median of around 25 days across their sixteen study catchments in France. Tian et al. (2020) obtained a median T_{opt} of 10 days for the top 70 cm layer using SMAP SSM across in situ SM monitoring sites in the Heihe River basin, China. Canadian agricultural areas are typically underrepresented in previous SWI-related studies, and hence the present study helps fill this gap. In this study, the obtained optimal T_{opt} values for the entire root zone (0–100 cm layer) at the watershed scale (~38 days) and for the majority of the 9-km grid cells (26 to 43 days) over the SNW are similar to those quantified in other agricultural regions (e.g., Bouaziz et al., 2020; Ceballos et al., 2005). The spatial variability of 9-km scale T_{opt} reasonably reflected the impact of soil texture. Note that at both scales (9-km and watershed) there is a range of T values surrounding T_{opt} that produce high correlations between the calculated SWI and modeled subsurface SM. As such, subsurface moisture variability over the SNW can be well represented by the SMAP-derived SWI using the classic T values (15 days and 20 days for the 0–20 cm and 0–100 cm layers, respectively). The analysis of optimal (and appropriate) time length T values in this study provide important guidance for SWI estimation over Canada and other agricultural regions around the world. Furthermore, GW storage showed a similar but slightly delayed day-to-day variation relative to SMAP-derived SWI in the 0–100 cm layer, which further supports the use of satellite-derived SWI for detecting GW changes over a range of different time scales (e.g., Sutanudjaja et al., 2013).

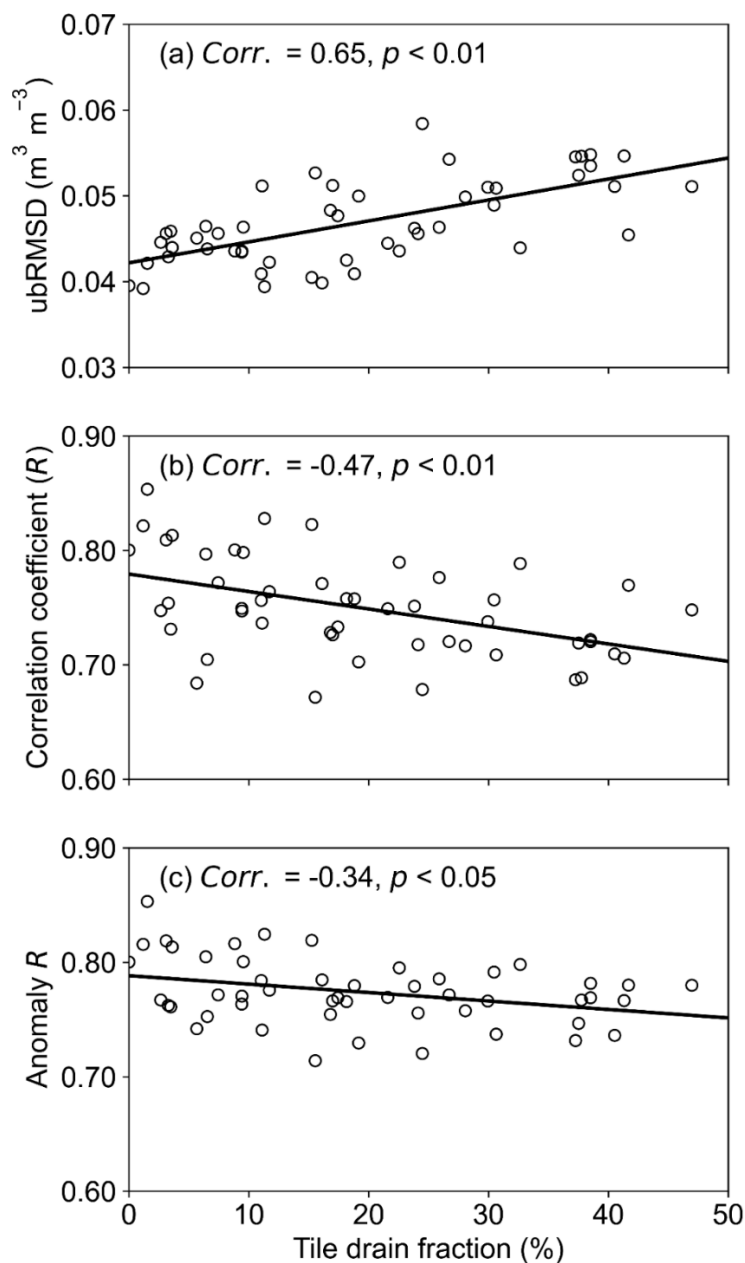
6.2 Limitations

Numerous modeling studies have demonstrated the influences of tile drains on hydrological behavior in tile-drained agricultural catchments or regions (e.g., De Schepper et al., 2015; Hansen et al., 2013; Que et al., 2015; Rozemeijer et al., 2010; Valayamkunnath et al., 2022). A limitation in the present study is that tile drainage was not explicitly resolved in the HGS model. However, this limitation is unavoidable, due to the extremely complex challenge associated with representing what are effectively a large number of field scale drainage features in a fully-integrated surface water – groundwater model for a ~ 3900 km² watershed. While HGS has previously been used to evaluate tile drainage impacts, the focus has been on much smaller (typically < 50 km²) catchments (e.g., Boico et al., 2022; De Schepper et al., 2015; 2017). To quantify the impact of tile drain omission on the study herein, the fraction of tile drains within each SMAP grid cell is calculated and evaluated in the context of the comparison between SMAP and HGS modeling.

Fig. 12 presents scatterplots of tile drain percentage versus calculated performance metrics for the SSM relationship between SMAP and the HGS modeling across all SMAP 9-km cells. The fraction of tile drains shows a statistically significant



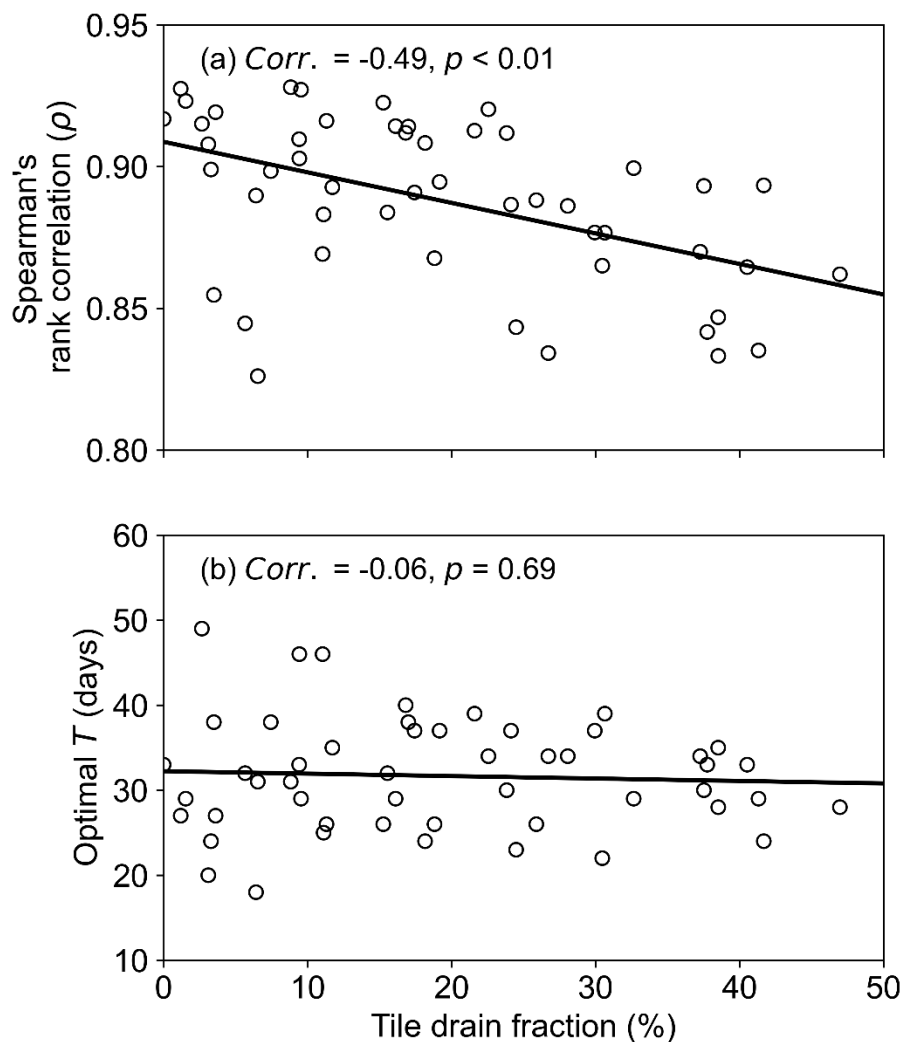
540 positive (negative) correlation with the ubRMSD (R and anomaly R). Further, Fig. 13a shows a scatterplot of tile drain
percentage versus maximum Spearman's rank correlation between SWI and simulated SM in the 0–100 cm layer, with there
being a statistically significant decrease in correlation strength as tile drainage increases. All these indicate that the lack of
tile drainage representation impacted the model performance over the tile drained areas, while also explaining the better
agreement between model simulations and SMAP (SSM and SWI) in forested areas than over agricultural fields (Figs. 3,
A10b, A10d, and A10f).



545



Figure 12: Scatterplot of the percent area of tile drains versus (a) ubRMSD, (b) R , and (c) anomaly R , respectively, across all SMAP grids within the SNW. The calculated performance metrics (shown in Fig. 3) were for HGS simulated SSM vs SMAP SSM. The Pearson correlation between tile drain fraction and each performance metric with p -value are provided in each plot.



550

Figure 13: Scatterplot of the percent area of tile drains versus (a) the highest Spearman's rank correlation between the SWI series and HGS 0–100 cm SM (as shown in Fig. A10f) and (b) the identified optimal T_{opt} value for the root zone layer (as shown in Fig. A10e) across all SMAP grids. In each plot, the Pearson correlation between the two variables with p -value are provided.

555 However, the tile sensitivity analysis also suggests that the tile drain omission would not negate the findings of the study since it is expected that agreement/linkages between SMAP and HGS modeling would be improved (rather than being discouraged) if tile drainage is explicitly included in the HGS model. Additionally, because the total tile-drained area is only about 25% of the entire watershed and the fraction of tile drains is less than 30% for the majority of SMAP grid cells (Fig.



12), the linkages between SMAP and fully-integrated surface water–groundwater modeling demonstrated within the results
560 of the study are till representative of the dynamic interplay between near surface–subsurface water over the study watershed.

The other limitation of the study is that the presence of tile drainage may impact accurate estimation of SWI over the SNW
through modifying the percolation process. However, the impact of this limitation is expected to be marginal for this study
given the following reasons. Firstly, the fraction of tile drainage is relatively low (< 30%) for most (80%) of the SMAP 9-km
565 grid cells (Fig. 13). Therefore, the tile drainage would not materially impact the percolation and the SWI estimation for most
of the 9-km grids. At the watershed scale, the percentage of total tile-drained area is only about 25% so that the estimation of
watershed-scale SWI should not be significantly influenced either. Secondly, the tile drainage has little impact upon the
identified T_{opt} , the only control parameter for the SWI estimation. In this study, T_{opt} was identified by matching the variations
in the SWI and simulated subsurface SM. Since the tile drainage was not resolved in the model, the identified T_{opt} and the
570 corresponding SWI estimation was not subject to the presence of tile drainage. Fig. 13b provides the scatterplot of the tile
drain percentage versus the identified optimal T_{opt} value for the SWI estimation in the 0–100 cm layer. The identified optimal
 T_{opt} did not exhibit a statistically significant variation with the fraction of tile drainage.

7. Conclusion

The inter-comparison and quantified linkage between the two independent data sources: SMAP measurements (SSM and
575 SWI) and HGS fully-integrated surface water – groundwater simulations over a representative agriculture-dominated
watershed in eastern Canada led to improved insights into the dynamics of near surface–subsurface water interaction and the
capabilities and approaches of satellite-based SM monitoring and high resolution fully-integrated hydrologic modeling. The
SSM variability is a strong reflection of the deeper subsurface water storage fluctuation, and results support the use of SMAP
SSM measurements as indicators and/or predictors of root zone SM and shallow GW storage dynamics. Furthermore, the
580 subsurface SM variability can be well represented by SMAP-derived SWI series, which can also be used to predict shallow
GW storage change. The vertical coupling strength and the time scale for water traveling from the near-surface to deeper
subsurface did not exhibit statistically significant differences across the two spatial scales of investigation, namely SMAP 9-
km grid cell and watershed. The high-resolution fully-integrated hydrologic simulations conducted with the HGS model
performed well in terms of reproducing the variably-saturated subsurface water dynamics, although adding the
585 representation of tile drains to the model would further improve the model performance for the tile-drained regions of the
subject watershed through the use of remote sensing based SM measurements as validation targets. As satellite SM
monitoring continues to evolve, this study has important implications for exploiting the potential of satellite-based SM to
predict root zone SM and GW dynamics.



Data Availability

590 The SMAP enhanced L3 radiometer 9 km EASE-grid soil moisture (SPL3SMP_E) version 5 product (O'Neill et al., 2021) and the model output from HydroGeoSphere (HGS) (Aquanty, 2022) were used in the creation of this manuscript. The data are publicly accessible at <https://doi.org/10.5281/zenodo.8145252> (Nayak et al., 2023).

Author contribution

AN, XX, and SF conceived the study. AN and XX analysed the data and wrote the manuscript draft. SF, OK, AE, DL, HR,
595 and ES contributed to the data curation, analysis and the editing of the manuscript.

Competing interests

The authors declare that they have no conflict of interest.

Acknowledgments

We acknowledge the support of the Canadian Space Agency (CSA) Grant 21SUESMVAS and the Canada 1 Water project.
600 Thanks go to the NASA National Snow and Ice Data Center Distributed Active Archive Center for providing access to the SMAP soil moisture product. Thanks also go to the South Nation Conservation Authority for providing the tile drain information.

References

- Ajami, H., Evans, J. P., McCabe, M. F., and Stisen, S.: Technical note: Reducing the spin-up time of integrated surface
605 water–groundwater models. *Hydrol. Earth Syst. Sci.*, 18 (12), 5169–5179. <https://doi.org/10.5194/hess-18-5169-2014>, 2014.
- Ajami, H., McCabe, M. F., and Evans, J. P.: Impacts of model initialization on an integrated surface water–groundwater model. *Hydro. Process.*, 29 (17), 3790–3801. <https://doi.org/10.1002/hyp.10478>, 2015.
- Al-Yaari, A., Wigneron, J.-P., Ducharne, A., Kerr, Y. H., Wagner, W., De Lannoy, G., et al.: Global-scale comparison of
610 passive (SMOS) and active (ASCAT) satellite based microwave soil moisture retrievals with soil moisture simulations (MERRA-Land). *Remote Sens. Environ.*, 152, 614–626. <https://doi.org/10.1016/j.rse.2014.07.013>, 2014.
- Albergel, C., Rüdiger, C., Pellarin, T., Calvet, J.-C., Fritz, N., Froissard, F., et al.: From near-surface to root-zone soil moisture using an exponential filter: an assessment of the method based on in-situ observations and model simulations. *Hydrol. Earth Syst. Sci.*, 12(6), 1323–1337. <https://doi.org/10.5194/hess-12-1323-2008>, 2008.



- 615 Aquanty: HydroGeoSphere: A three-dimensional numerical model describing fully integrated subsurface and surface flow and solute transport. Waterloo, ON, 2022.
- Aziz, T., Frey, S. K., Lapen, D. R., Preston, S., Russell, H. A. J., Khader, O., Erler, A. R., and Sudicky, E. A.: Monetizing the role of water in sustaining watershed ecosystem services using a fully integrated subsurface–surface water model, *Hydrol. Earth Syst. Sci. Discuss.* <https://doi.org/10.5194/hess-2023-25>, in review, 2023.
- 620 Bartalis, Z., Wagner, W., Naeimi, V., Hasenauer, S., Scipal, K., Bonekamp, H., et al. : Initial soil moisture retrievals from the METOP-A Advanced Scatterometer (ASCAT), *Geophys. Res. Lett.*, 34(20), L20401. <https://doi.org/10.1029/2007GL031088>, 2007.
- Boico, V.F., Therrien, R., Delottier, H., Young, N. L. and Højberg, A.L.: Comparing alternative conceptual models for tile drains and soil heterogeneity for the simulation of tile drainage in agricultural catchments, *J. Hydrol.*, 612, 128120. <https://doi.org/10.1016/j.jhydrol.2022.128120>, 2022.
- 625 Bouaziz, L. J. E., Steele-Dunne, S. C., Schellekens, J., Weerts, A. H., Stam, J., Sprokkereef, E., et al.: Improved Understanding of the Link Between Catchment-Scale Vegetation Accessible Storage and Satellite-Derived Soil Water Index, *Water Resour. Res.*, 56(3), e2019WR026365. <https://doi.org/10.1029/2019WR026365>, 2020.
- Ceballos, A., Scipal, K., Wagner, W., and Martínez-Fernández, J.: Validation of ERS scatterometer-derived soil moisture data in the central part of the Duero Basin, Spain, *Hydro. Process.*, 19(8), 1549–1566. <https://doi.org/10.1002/hyp.5585>, 2005.
- 630 Colliander, A., and Coauthors: Validation of SMAP surface soil moisture products with core validation sites, *Remote Sens. Environ.*, 191, 215–231, doi:10.1016/j.rse.2017.01.021, 2017.
- de Lange, R., Beck, R., van de Giesen, N., Friesen, J., de Wit, A., and Wagner, W.: Scatterometer-derived soil moisture calibrated for soil texture with a one-dimensional water-flow model. *IEEE Transactions on Geoscience and Remote Sensing*, 46(12), 4041–4049. <https://doi.org/10.1109/TGRS.2008.2000796>, 2008.
- De Schepper, G., Therrien, R., Refsgaard, J.C., and Hansen, A.L.: Simulating coupled surface and subsurface water flow in a tile-drained agricultural catchment. *J. Hydrol.* , 521, 374–388. <https://doi.org/10.1016/j.jhydrol.2014.12.035>, 2015.
- De Schepper, G., Therrien, R., Refsgaard, J. C., He, X., Kjaergaard, C., and Iversen, B. V.: Simulating seasonal variations of tile drainage discharge in an agricultural catchment, *Water Resour. Res.*, 53, 3896–3920. <https://doi.org/10.1002/2016WR020209>, 2017.
- 640 Dorigo, W. A., Scipal, K., Parinussa, R. M., Liu, Y. Y., Wagner, W., de Jeu, R. A. M., and Naeimi, V.: Error characterisation of global active and passive microwave soil moisture datasets. *Hydrol. Earth Syst. Sci.*, 14(12), 2605–2616. <https://doi.org/10.5194/hess-14-2605-2010>, 2010.
- 645 Dobriyal, P., Qureshi, A., Badola, R., and Hussain, S.A.: A review of the methods available for estimating soil moisture and its implications for water resource management, *J. Hydrol.*, 458–459, 110–117. <https://doi.org/10.1016/j.jhydrol.2012.06.021>, 2012.



- Draper, C., Reichle, R., de Jeu, R., Naeimi, V., Parinussa, R., and Wagner, W.: Estimating root mean square errors in remotely sensed soil moisture over continental scale domains. *Remote Sens. Environ.*, 137, 288–298. <https://doi.org/10.1016/j.rse.2013.06.013>, 2013.
- Entekhabi, D., Njoku, E. G., O’Neill, P. E., Kellogg, K. H., Crow, W. T., Edelstein, W. N., et al.: The Soil Moisture Active Passive (SMAP) mission. *Proceedings of the IEEE*, 98(5), 704–716. <https://doi.org/10.1109/JPROC.2010.2043918>, 2010.
- Erdal, D., Baroni, G., Sánchez-León, E., and Cirpka, O. A.: The value of simplified models for spin up of complex models with an application to subsurface hydrology. *Computers and Geosciences*, 126, 62–72. <https://doi.org/10.1016/j.cageo.2019.01.014>, 2019.
- Erler, A.R., Frey, S.K., Khader, O., d’Orgeville, M., Park, Y., Hwang, H., Lapen, D.R., Peltier, W.R., and Sudicky, E.A. (2019). Evaluating climate change impacts on soil moisture and groundwater resources within a lake-affected region, *Water Resour. Res.*, 55 (10), 8142–8163. <https://doi.org/10.1029/2018WR023822>, 2019.
- Famiglietti, J. S., Lo, M., Ho, S. L., Bethune, J., Anderson, K. J., Syed, T. H., et al.: Satellites measure recent rates of groundwater depletion in California’s Central Valley, *Geophys. Res. Lett.*, 38(3), 2010GL046442. <https://doi.org/10.1029/2010GL046442>, 2011.
- Ford, T.W., Harris, E., and Quiring, S. M.: Estimating root zone soil moisture using near-surface observations from SMOS. *Hydrol. Earth Syst. Sci.*, 18(1), 139–154. <https://doi.org/10.5194/hess-18-139-2014>, 2014.
- Frey, S. K., Miller, K., Khader, O., Taylor, A., Morrison, D., Xu, X., et al.: Evaluating landscape influences on hydrologic behavior with a fully-integrated groundwater – surface water model. *J. Hydrol.*, 602, 126758. <https://doi.org/10.1016/j.jhydrol.2021.126758>, 2021.
- Hansen, A. L., Refsgaard, J. C., Christensen, B. S. B., and Jensen, K. H.: Importance of including small-scale tile drain discharge in the calibration of a coupled groundwater-surface water catchment model. *Water Resour. Res.*, 49, 585–603. <https://doi.org/10.1029/2011WR011783>, 2013.
- Hwang, H. T., Park, Y. J., Sudicky, E., and Forsyth, P. A.: A parallel computational framework to solve flow and transport in integrated surface–subsurface hydrologic systems. *Environmental Modelling and Software*, 61, 39–58. [doi:10.1016/j.envsoft.2014.06.024](https://doi.org/10.1016/j.envsoft.2014.06.024), 2014.
- Jonard, F., Bogena, H., Caterina, D., Garré, S., Klotzsche, A., Moneris, A., et al.: Ground-based soil moisture determination. In *Observation and Measurement of Ecohydrological Processes* (pp. 1–42). Springer, Berlin, Heidelberg. https://doi.org/10.1007/978-3-662-47871-4_2-1, 2018.
- Kerr, Y. H., Waldteufel, P., Wigneron, J.-P., Delwart, S., Cabot, F., Boutin, J., et al.: The SMOS mission: New tool for monitoring key elements of the global water cycle. *Proceedings of the IEEE*, 98(5), 666–687. <https://doi.org/10.1109/JPROC.2010.2043032>, 2010.
- Logan, C., Cummings, D. I., Pullan, S., Pugin, A., Russell, H. A. J., and Sharpe, D. R.: Hydrostratigraphic model of the South Nation watershed region, south-eastern Ontario, Geological Survey of Canada, 17 pp., <https://doi.org/10.4095/248203>, 2009.



- Mahmood, R., Littell, A., Hubbard, K.G., and You, J.: Observed data-based assessment of relationships among soil moisture at various depths, precipitation, and temperature. *Applied Geography*, 34, 255–264. <https://doi.org/10.1016/j.apgeog.2011.11.009>, 2012.
- 685 Mahmood, R., and Hubbard, K. G.: Relationship between soil moisture of near surface and multiple depths of the root zone under heterogeneous land uses and varying hydroclimatic conditions. *Hydrological Processes*, 21, 3449–3462. <https://doi.org/10.1002/hyp.6578>, 2007.
- Manfreda, S., Brocca, L., Moramarco, T., Melone, F., and Sheffield, J.: A physically based approach for the estimation of root-zone soil moisture from surface measurements. *Hydrol. Earth Syst. Sci.*, 18, 1199–1212.
- 690 <https://doi.org/10.5194/hess-18-1199-2014>, 2014.
- McKenney, D. W., Hutchinson, M. F., Papadopol, P., Lawrence, K., Pedlar, J., Campbell, K., et al.: Customized spatial climate models for North America. *Bulletin of the American Meteorological Society*, 92(12), 1611–1622. <https://doi.org/10.1175/2011bams3132.1>, 2011.
- Muñoz-Sabater, J., Dutra, E., Agustí-Panareda, A., Albergel, C., Arduini, G., Balsamo, G., Boussetta, S., Choulga, M., 695 Harrigan, S., Hersbach, H., Martens, B., Miralles, D. G., Piles, M., Rodríguez-Fernández, N. J., Zsoter, E., Buontempo, C., and Thépaut, J. N.: ERA5-Land: A state-of-the-art global reanalysis dataset for land applications, *Earth Syst. Sci. Data*, 13, 4349–4383, <https://doi.org/10.5194/essd-13-4349-2021>, 2021.
- Nayak, A.K., Biswal, B., and Sudheer, K.P.: A novel framework to determine the usefulness of satellite-based soil moisture data in streamflow prediction using dynamic Budyko model. *J. Hydrol.*, 595, 125849.
- 700 <https://doi.org/10.1016/j.jhydrol.2020.125849>, 2021.
- Nayak, A.K., Xu, X., Frey, S.K., Khader, O., Eler, A.R., Lapen, D.R., Russell, H.A.J., and Sudicky, E.A.: Quantifying the linkage between SMAP soil moisture and fully-integrated hydrologic simulations [Dataset]. Zenodo. <https://doi.org/10.5281/zenodo.8145252>, 2023.
- Njoku, E. G., Jackson, T. J., Lakshmi, V., Chan, T. K., and Nghiem, S. V.: Soil moisture retrieval from AMSR-E. *IEEE Transactions of Geosciences and Remote Sensing*, 41, 215–228. <https://doi.org/10.1109/TGRS.2002.808243>, 2003.
- 705 O’Neill, P.E., Chan, S., Njoku, E.G., Jackson, T., Bindlish, R., Chaubell, J., and Colliander, A. (2021). SMAP enhanced L3 radiometer global and polar grid daily 9 km EASE-grid soil moisture, version 5. NASA National Snow and Ice Data Center Distributed Active Archive Center, Boulder, CO, USA. <https://doi.org/10.5067/4DQ54OUIJ9DL>, 2021.
- Owe, M., de Jeu, R., and Holmes, T.: Multisensor historical climatology of satellite-derived global land surface moisture. *Journal of Geophysical Research*, 113, F01002. <https://doi.org/10.1029/2007JF000769>, 2008.
- 710 Parrens, M., Zakharova, E., Lafont, S., Calvet, J.-C., Kerr, Y., Wagner, W., and Wigneron, J.-P.: Comparing soil moisture retrievals from SMOS and ASCAT over France. *Hydrol. Earth Syst. Sci.*, 16, 423–440. <https://doi.org/10.5194/hess-16-423-2012>, 2012.



- Paulik, C., Dorigo, W., Wagner, W., and Kidd, R.: Validation of the ASCAT Soil Water Index using in situ data from the
715 International Soil moisture network. *International Journal of Applied Earth Observation and Geoinformation*, 30(1), 1–8.
<https://doi.org/10.1016/j.jag.2014.01.007>, 2014.
- Que, Z., Seidou, O., Droste, R.L., Wilkes, G., Sunohara, M., Topp, E. and Lapen, D.R.: Using AnnAGNPS to predict the
effects of tile drainage control on nutrient and sediment loads for a river basin. *Journal of Environmental Quality*, 44(2),
629–641. <https://doi.org/10.2134/jeq2014.06.0246>, 2015.
- 720 Ragab, R.: Towards a continuous operational system to estimate the root-zone soil moisture from intermittent remotely
sensed surface moisture. *J. Hydrol.*, 173(1-4), 1–25. [https://doi.org/10.1016/0022-1694\(95\)02749-F](https://doi.org/10.1016/0022-1694(95)02749-F), 1995.
- Rodell, M., Chen, J., Kato, H., Famiglietti, J. S., Nigro, J., and Wilson, C. R.: Estimating groundwater storage changes in the
Mississippi River basin (USA) using GRACE. *Hydrogeology Journal*, 15, 159–166. <https://doi.org/10.1007/s10040-006-0103-7>, 2007.
- 725 Rodell, M., Velicogna, I. and Famiglietti, J. S.: Satellite-based estimates of groundwater depletion in India. *Nature*, 460,
999–1002, 2009.
- Rodell, M., Famiglietti, J. S., and Wiese, D. N.: Emerging trends in global freshwater availability. *Nature*, 557, 651–659.
<https://doi.org/10.1038/s41586-018-0123-1>, 2018.
- Rozemeijer, J. C., van der Velde, Y., McLaren, R. G., van Geer, F. C., Broers, H. P., and Bierkens, M. F. P.: Integrated
730 modeling of groundwater-surface water interactions in a tile-drained agricultural field: The importance of directly
measured flow route contributions. *Water Resour. Res.*, 46(11). <https://doi.org/10.1029/2010WR009155>, 2010.
- Simmons, C.T., Brunner, P., Therrien, R. and Sudicky, E. A.: Commemorating the 50th anniversary of the Freeze and Harlan
(1969) Blueprint for a physically-based, digitally-simulated hydrologic response model. *J. Hydrol.*, 584, 124309.
<https://doi.org/10.1016/j.jhydrol.2019.124309>, 2020.
- 735 Singh, G., Panda, R. K., and Mohanty, B. P.: Spatiotemporal Analysis of Soil Moisture and Optimal Sampling Design for
Regional-Scale Soil Moisture Estimation in a Tropical Watershed of India. *Water Resour. Res.*, 55, 2057–2078.
<https://doi.org/10.1029/2018WR024044>, 2019.
- Sunohara, M.D., Gottschall, N., Wilkes, G., Craiovan, E., Topp, E., Que, Z., Seidou, O., Frey, S.K., and Lapen, D.R.: Long-
term observations of nitrogen and phosphorus export in paired-agricultural watersheds under controlled and conventional
740 tile drainage. *Journal of environmental quality*, 44(5), 1589–1604. <https://doi.org/10.2134/jeq2015.01.0008>, 2015.
- Sutanudjaja, E. H., de Jong, S. M., van Geer, F. C., and Bierkens, M. F. P.: Using ERS spaceborne microwave soil moisture
observations to predict groundwater head in space and time. *Remote Sens. Environ.*, 138, 172–188.
<https://doi.org/10.1016/j.rse.2013.07.022>, 2013.
- Syed, T. H., Famiglietti, J. S., Rodell, M., Chen, J., and Wilson, C. R.: Analysis of terrestrial water storage changes from
745 GRACE and GLDAS. *Water Resour. Res.*, 44(2). <https://doi.org/10.1029/2006WR005779>, 2008.
- Tapley, B. D., Bettadpur, S., Ries, J. C., Thompson, P. F., and Watkins, M. M.: GRACE measurements of mass variability in
the earth system. *Science*, 305(5683), 503–505. <https://doi.org/10.1126/science.1099192>, 2004.



- Tian, J., Han, Z., Bogena, H. R., Huisman, J. A., Montzka, C., Zhang, B., and He, C.: Estimation of subsurface soil moisture from surface soil moisture in cold mountainous areas. *Hydrol. Earth Syst. Sci.*, 24(9), 4659–4674.
750 <https://doi.org/10.5194/hess-24-4659-2020>, 2020.
- Thomas, B. F., and Famiglietti, J. S.: Identifying climate-induced groundwater depletion in GRACE observations. *Scientific Reports*, 9, 4124. <https://doi.org/10.1038/s41598-019-40155-y>, 2019.
- Valayamkunnath, P., Gochis, D. J., Chen, F., Barlage, M., and Franz, K. J.: Modeling the hydrologic influence of subsurface tile drainage using the National Water Model. *Water Resour. Res.*, 58(4). <https://doi.org/10.1029/2021WR031242>, 2022.
- 755 Wagner, W., Lemoine, G., and Rott, H.: A method for estimating soil moisture from ERS Scatterometer and soil data. *Remote Sens. Environ.*, 70(2), 191–207. [https://doi.org/10.1016/S0034-4257\(99\)00036-X](https://doi.org/10.1016/S0034-4257(99)00036-X), 1999.
- Wang, T., Franz, T. E., You, J., Shulski, M. D., and Ray, C.: Evaluating controls of soil properties and climatic conditions on the use of an exponential filter for converting near surface to root zone soil moisture contents. *J. Hydrol.*, 548, 683–696. <https://doi.org/10.1016/j.jhydrol.2017.03.055>, 2017.
- 760 Wu, W., Geller, M. A., and Dickinson, R. E.: The response of soil moisture to long-term variability of precipitation. *J. Hydrometeorol.*, 3(5), 604–613. [https://doi.org/10.1175/1525-7541\(2002\)003<0604:TROSMT>2.0.CO;2](https://doi.org/10.1175/1525-7541(2002)003<0604:TROSMT>2.0.CO;2), 2002.
- Xu, S., Frey, S. K., Erler, A. R., Khader, O., Berg, S. J., Hwang, H. T., et al.: Investigating groundwater-lake interactions in the Laurentian Great Lakes with a fully-integrated surface water-groundwater model. *J. Hydrol.*, 594, 125911. <https://doi.org/10.1016/j.jhydrol.2020.125911>, 2021.
- 765 Xu, X., Li, J., and Tolson, B. A.: Progress in integrating remote sensing data and hydrologic modeling. *Prog. Phys. Geogr.*, 38(4), 464–498. <https://doi.org/10.1177/0309133314536583>, 2014.
- Xu, X.: Evaluation of SMAP level 2, 3, and 4 soil moisture datasets over the Great Lakes region. *Remote Sens.*, 12(22), 3785. <https://doi.org/10.3390/rs12223785>, 2020.
- Xu, X., and Frey, S.K.: Validation of SMOS, SMAP, and ESA CCI soil moisture over a humid region. *IEEE Journal of Selected Topics in Applied Earth Observations and Remote Sensing*, 14, 10784–10793. <https://doi.org/10.1109/JSTARS.2021.3122068>, 2021.
- 770 Zhang, N., Quiring, S., Ochsner, T., and Ford, T.: Comparison of three methods for vertical extrapolation of soil moisture in Oklahoma. *Vadose Zone Journal*, 16(10), vzt2017.04.0085. <https://doi.org/10.2136/vzt2017.04.0085>, 2017.
- Zhao, D., Kuenzer, C., Fu, C., and Wagner, W.: Evaluation of the ERS Scatterometer-Derived Soil Water Index to Monitor Water Availability and Precipitation Distribution at Three Different Scales in China, *J. Hydrometeorol.*, 9(3), 549–562. <https://doi.org/10.1175/2007JHM965.1>, 2008.
- 775 Zhu, Y., Myint, S.W., Schaffer-Smith, D., Sauchyn, D.J., Xu, X., Piwowar, J. M., and Li, Y.: Examining ground and surface water changes in response to environmental variables, land use dynamics, and socioeconomic changes in Canada, *J. Environ. Manage.*, 322, 115875. <https://doi.org/10.1016/j.jenvman.2022.115875>, 2022.

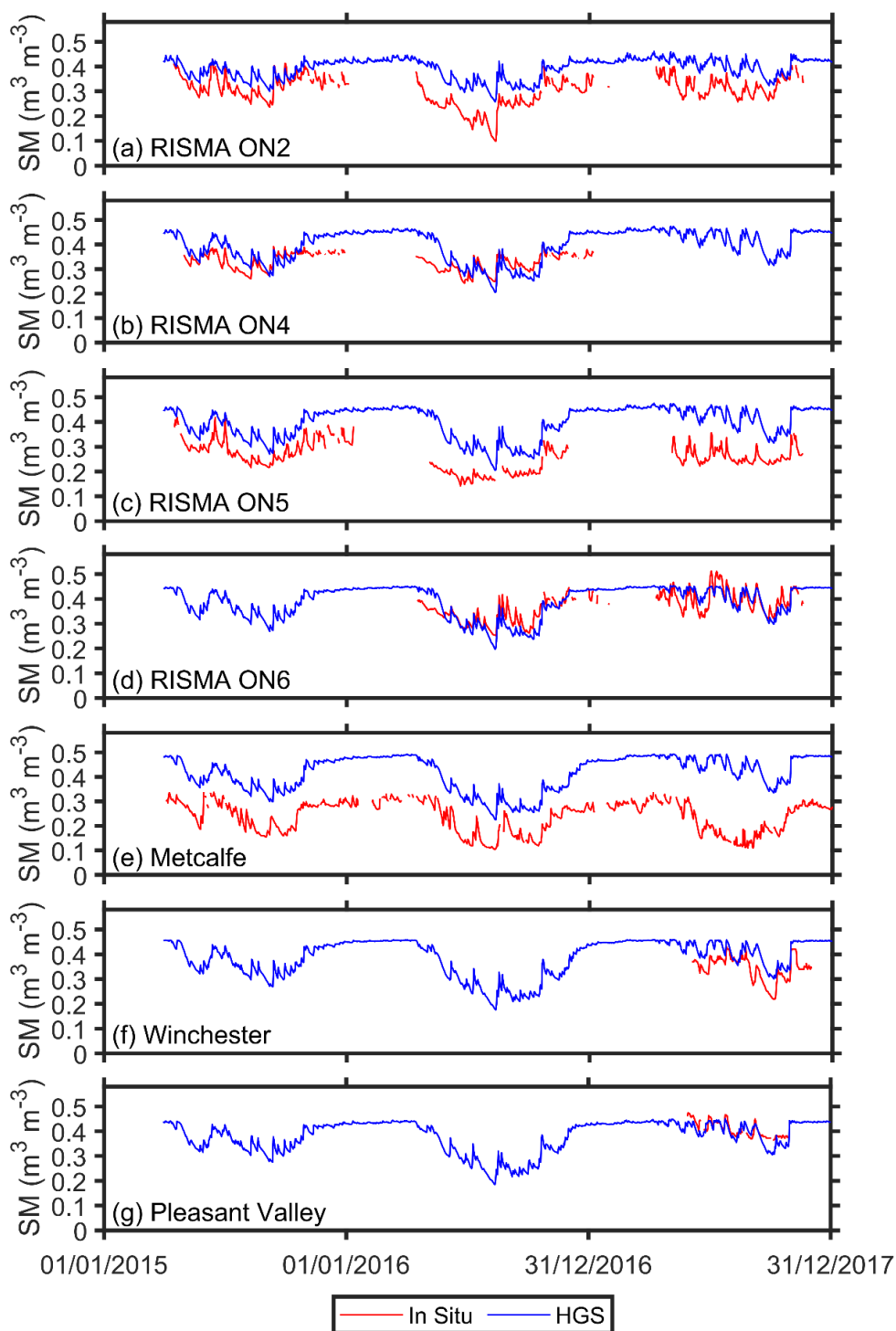


Appendix A

Table A1. Specification of in situ soil moisture stations

Station ID	Latitude (°)	Longitude (°)	Sampling Intervals	Measuring Depths (cm)	Data Period
^a RISMA ON2	45.4016	-74.9479	15 mins	0-5, 5, 20, 50	2015 to 2017
RISMA ON4	45.3140	-75.0193	15 mins	0-5, 5, 20, 50	2015 to 2016
RISMA ON5	45.3769	-75.0031	15 mins	0-5, 5, 20, 50, 100	2015 to 2017
RISMA ON6	45.3628	-74.9342	15 mins	0-5, 5, 20, 50	2016 to 2017
Metcalfe	45.2626	-75.3439	Hourly	10, 20	2015 to 2017
Pleasant Valley	44.9726	-75.4237	Hourly	10, 20, 50	2017
^b WEBs@11-14	45.2598	-75.1929	15 mins	15, 45	2015 to 2017
WEBs@20	45.2639	-75.1607	15 mins	15, 45	2015 to 2017
Winchester	45.0623	-75.3418	Hourly	20	2017

- 785 a. Agriculture and Agri-Food Canada's Ontario Real-Time In-Situ Soil Monitoring for Agriculture (RISMA) stations
 b. Agriculture and Agri-Food Canada's WEBs meteorological stations



790 **Figure A1:** The 0-25 cm depth soil moisture time series of HGS versus In Situ at (a) ON2, (b) ON4, (c) ON5, (d) ON6, (e) Metcalfe, (f) Winchester, and (g) Pleasant Valley, respectively.

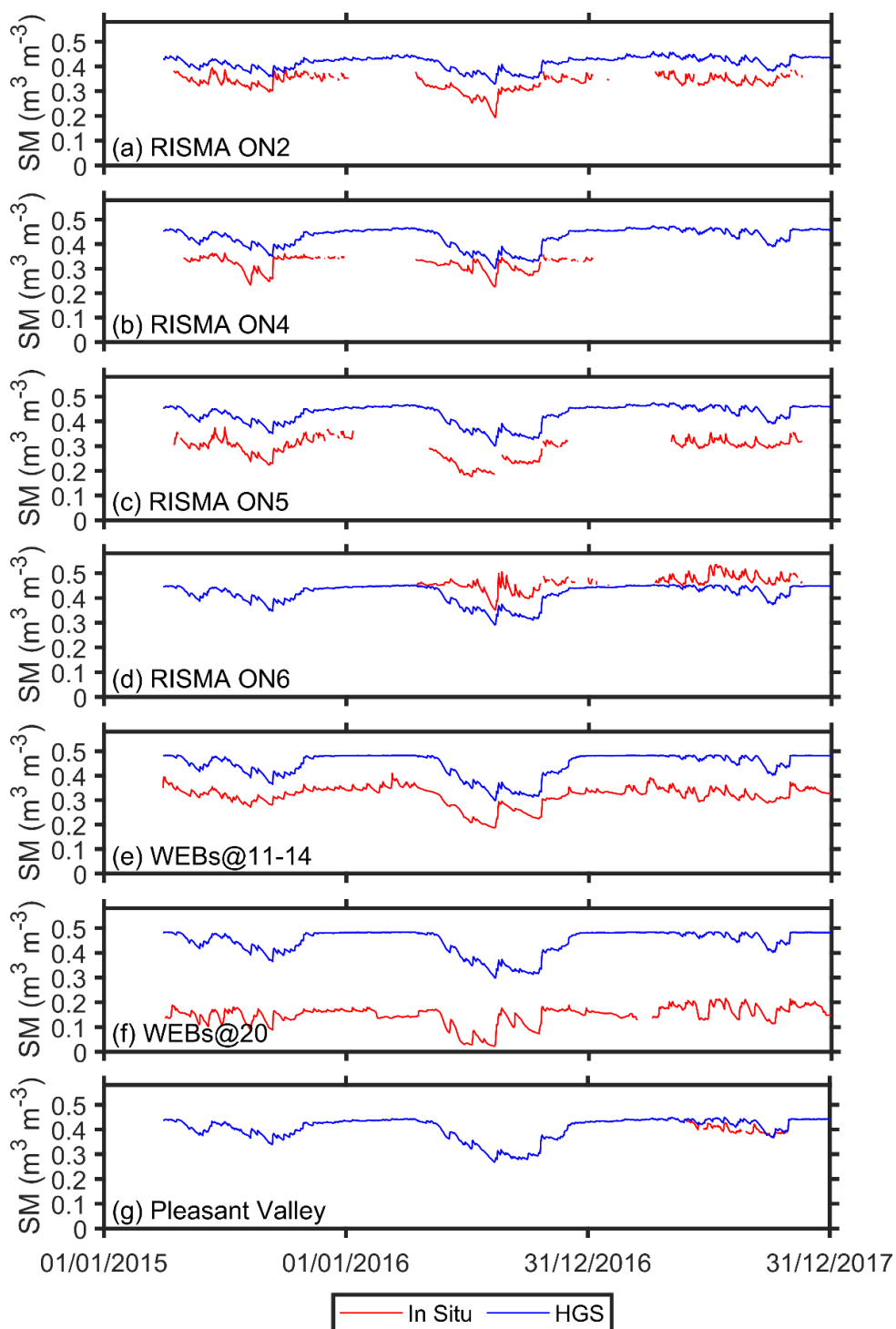
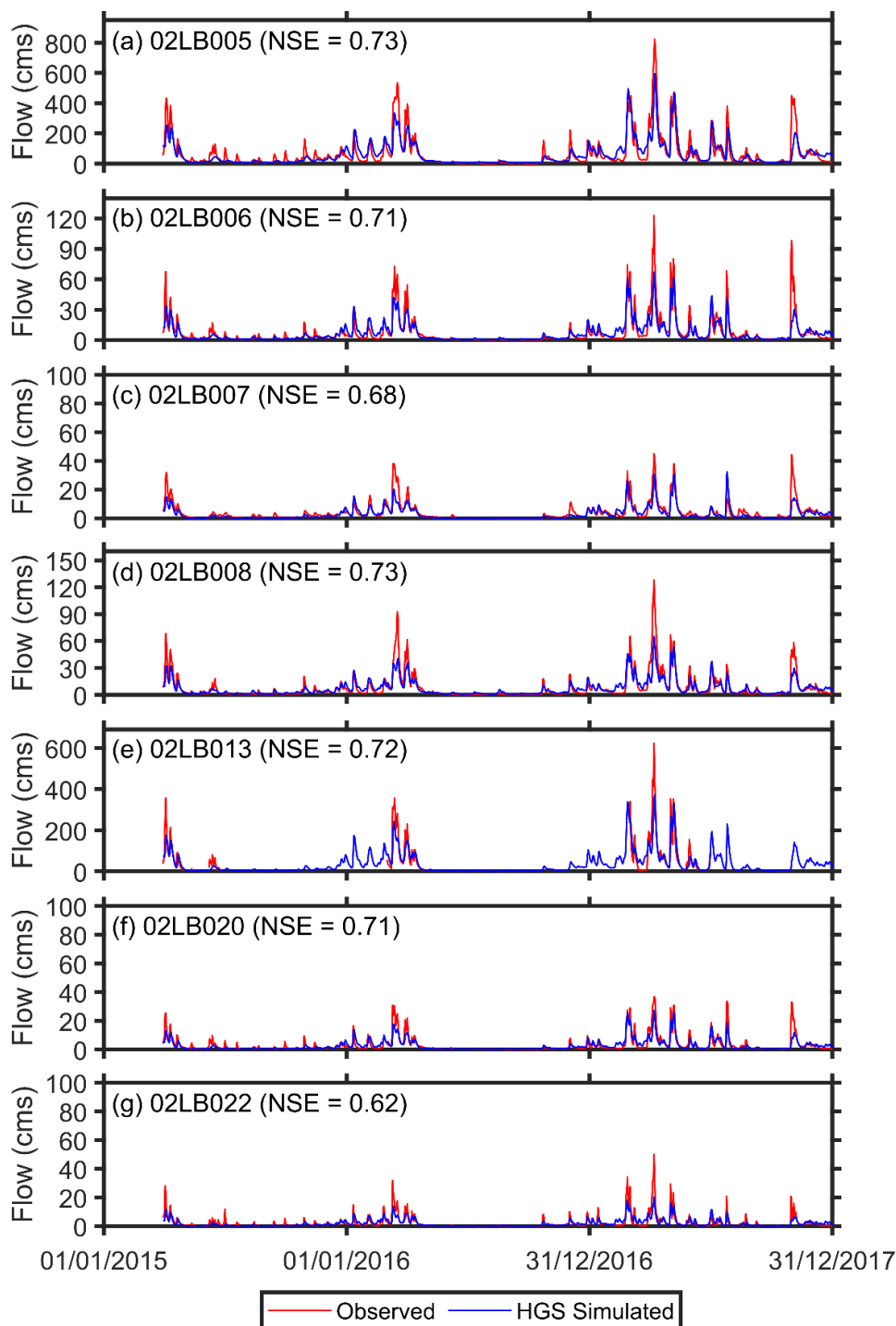
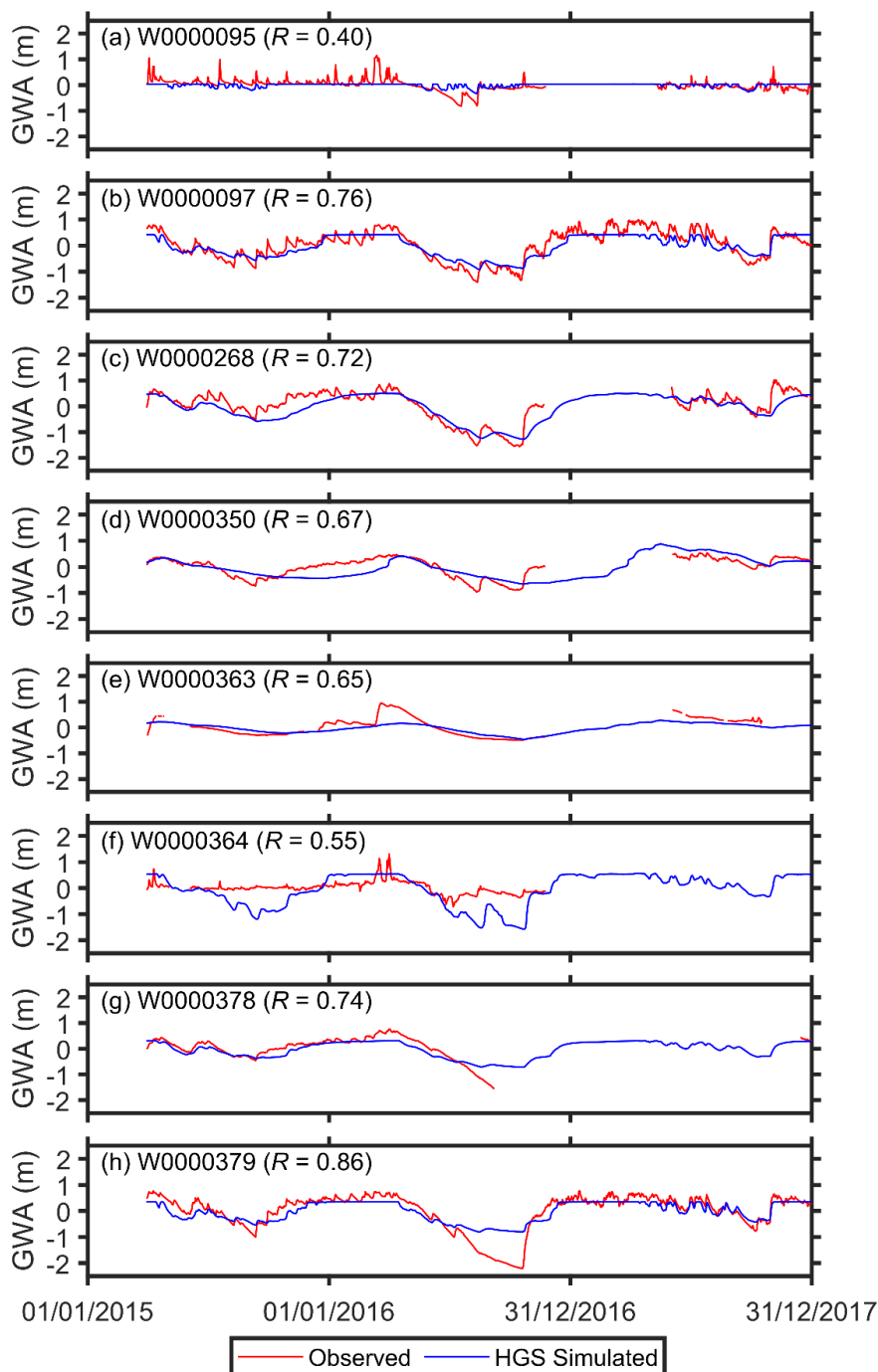


Figure A2. The 0-100 cm depth soil moisture time series of HGS versus In Situ at (a) ON2, (b) ON4, (c) ON5, (d) ON6, (e) WEBs@11-14, (f) WEBs@20, and (g) Pleasant Valley, respectively.



795

Figure A3: Comparison between the observed and HGS simulated hydrographs at the seven gauges: (a) 02LB005, (b) 02LB006, (c) 02LB007, (d) 02LB008, (e) 02LB013, (f) 02LB020, and (g) 02LB022, respectively. The corresponding Nash-Sutcliffe efficiency (NSE) value is provided in each panel.

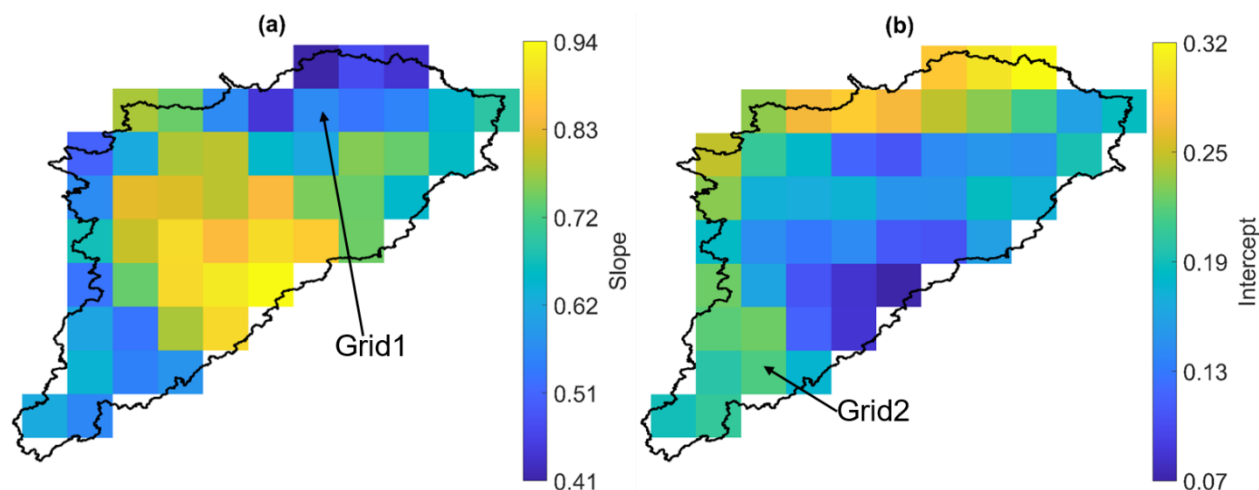


800

Figure A4: Comparison between the observed and HGS simulated groundwater level anomalies (GWA) at the eight GW monitoring wells. The anomalies represent the deviations relative to their respective means over the study period. The corresponding R value is provided in each panel.



805



Figures A5: (a) Slope and (b) intercept for a linear regression between SMAP SSM (independent variable) versus HGS SSM (dependent variable) across all SMAP grids.

810

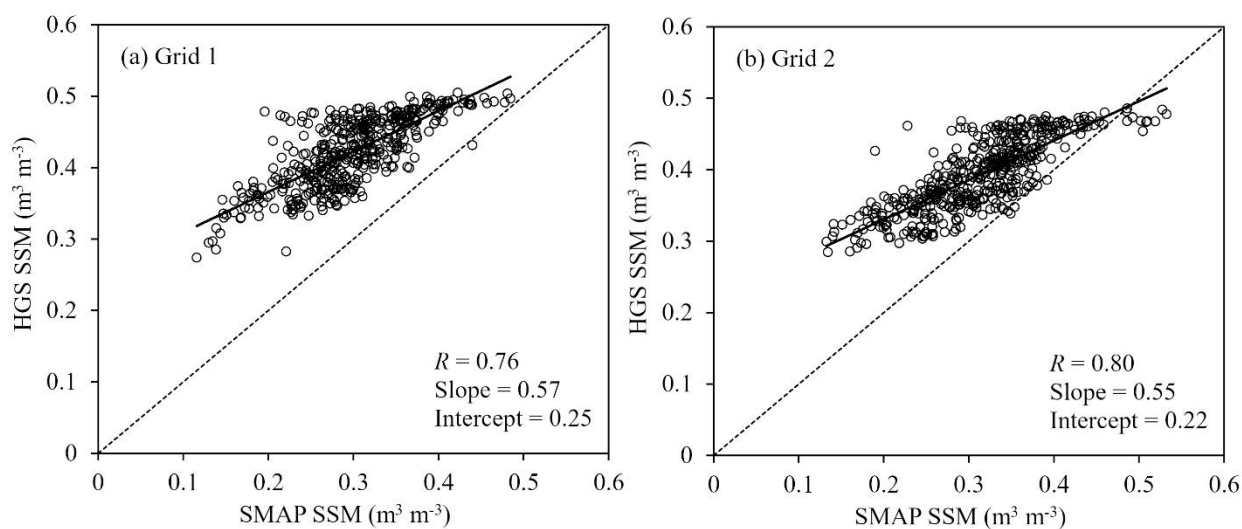
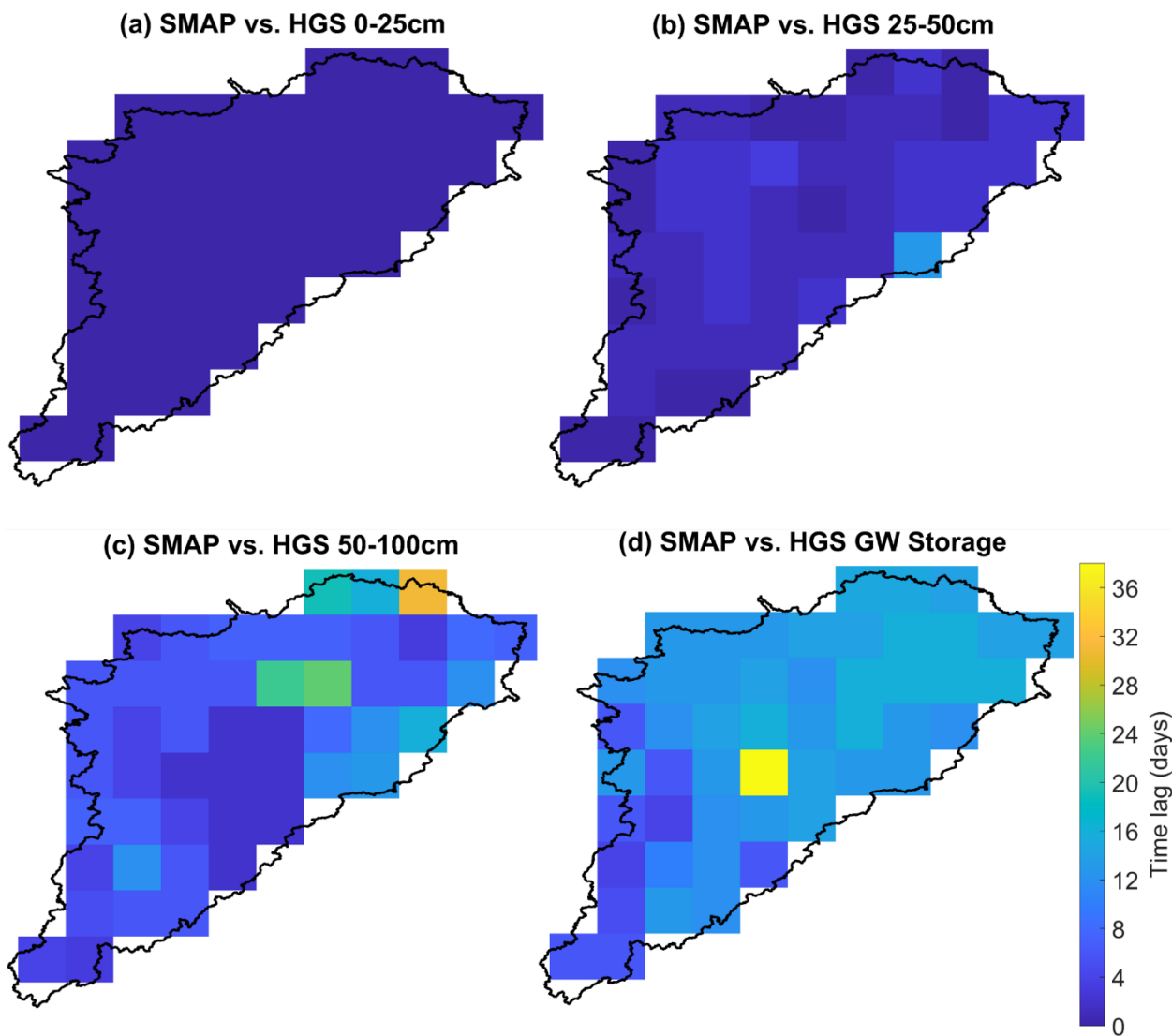
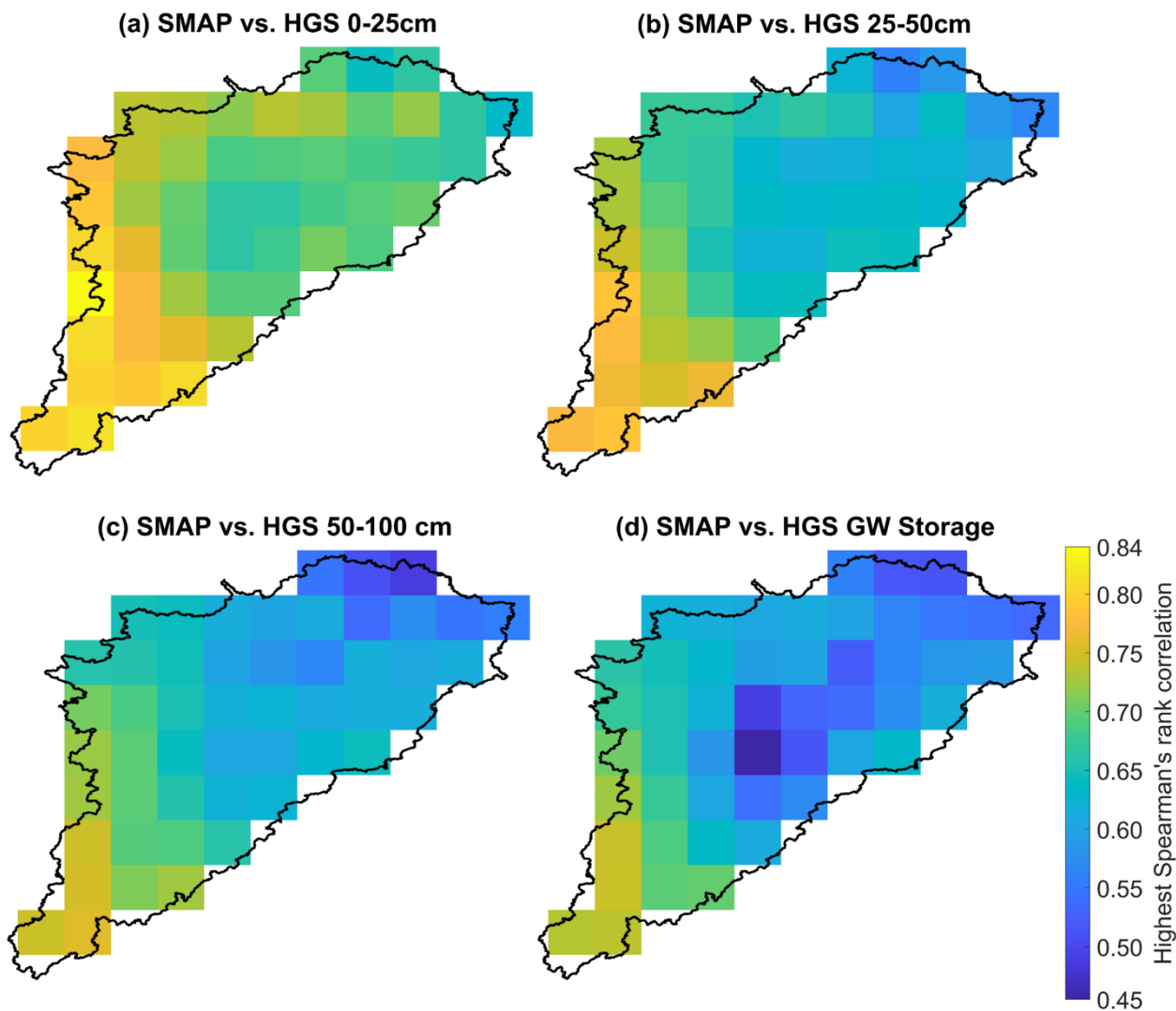


Figure A6: Scatterplots between SMAP SSM and HGS SSM for (a) Grid 1 and (b) Grid 2, as shown in Figure A5.



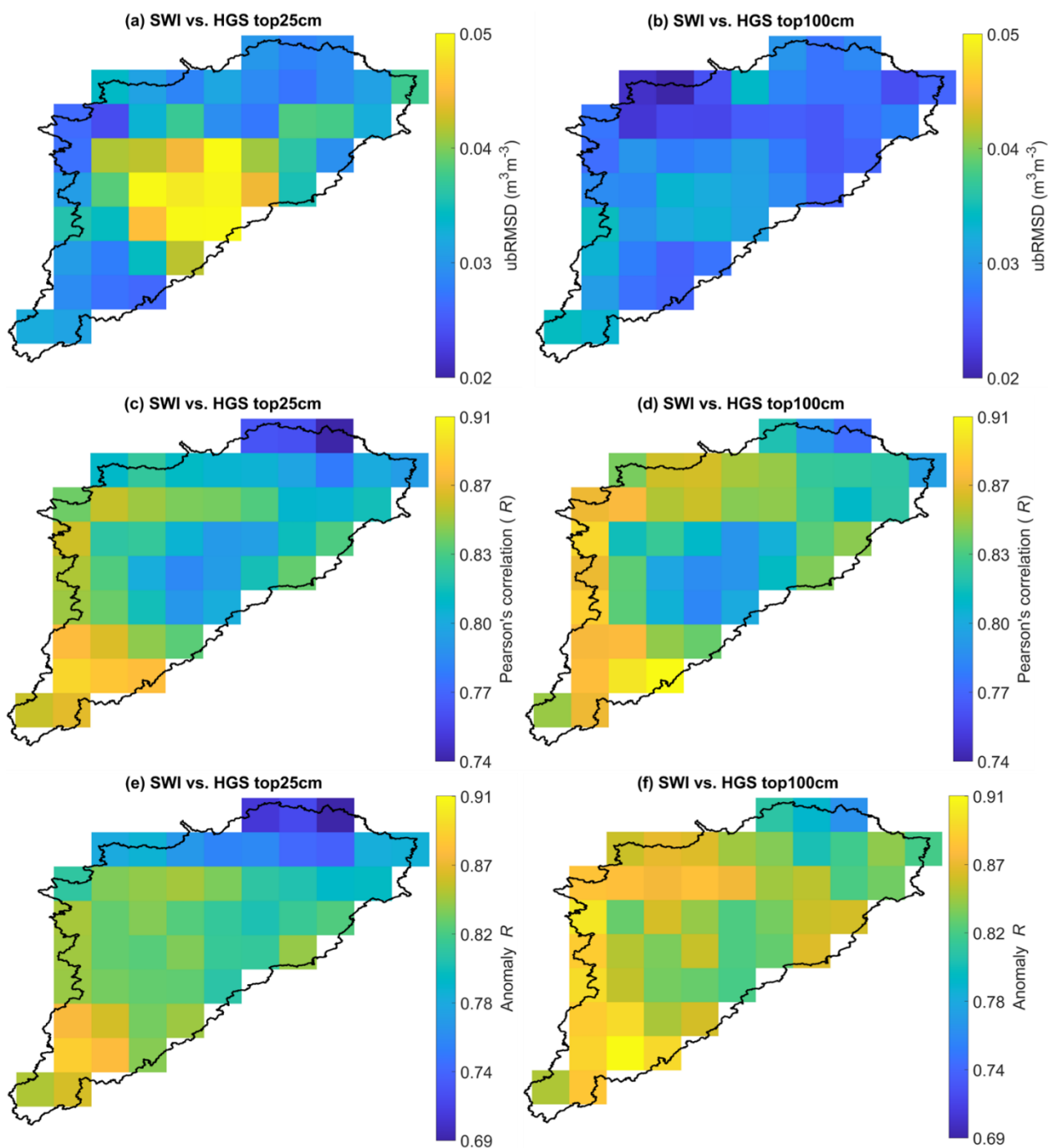
815

Figures A7: Optimal time lag (in days), relative to the SMAP SSM variability, for HGS simulated (a) 0–25 cm SM, (b) 25–50 cm SM, (c) 50–100 cm SM, and (d) GW storage across all SMAP grids.

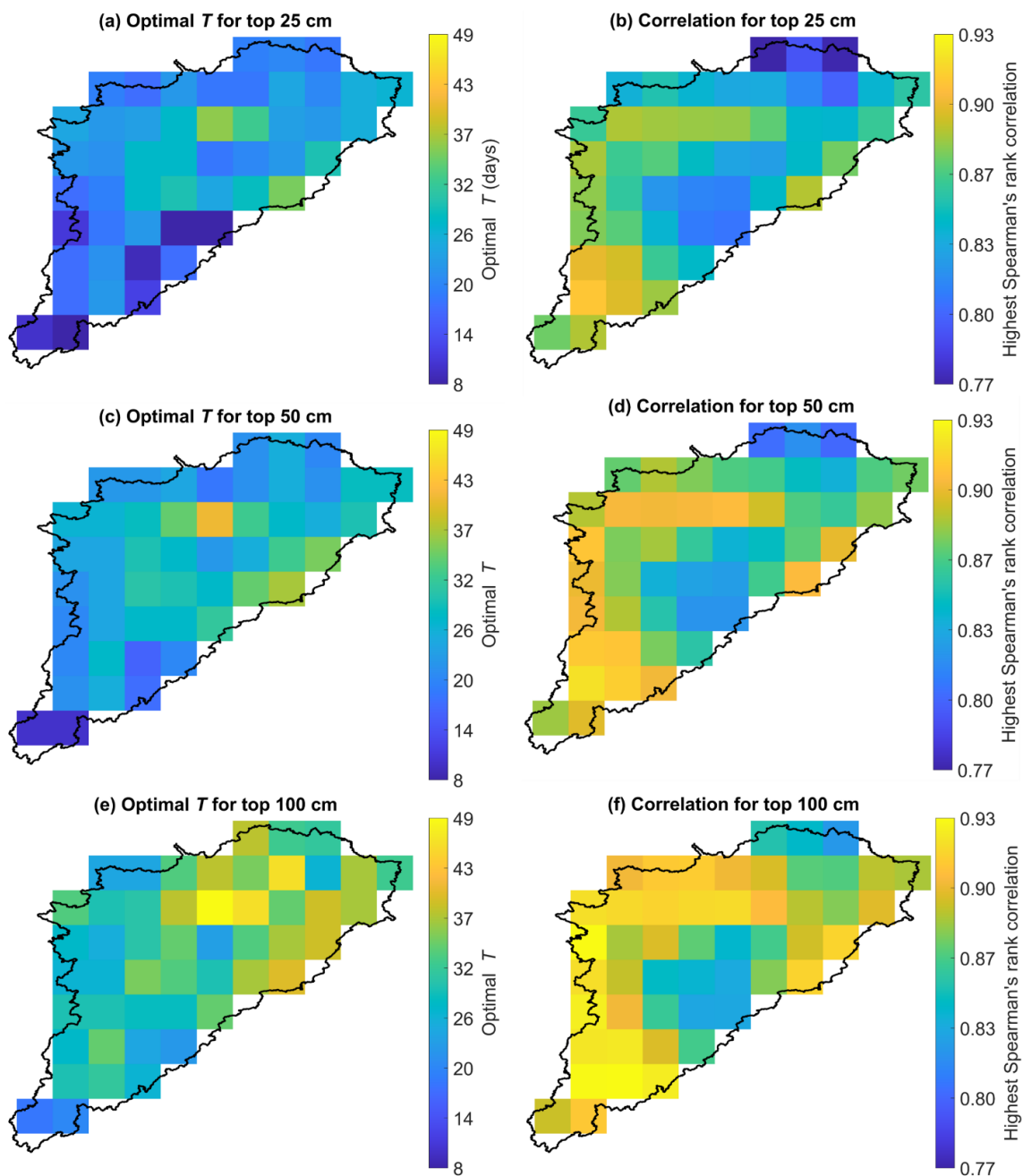


820 **Figures A8:** Maximum Spearman's rank correlation between SMAP SSM versus HGS simulated (a) 0–25 cm SM, (b) 25–50 cm SM, (c)
825 50–100 cm SM, and (d) GW storage, respectively, across all SMAP grids.

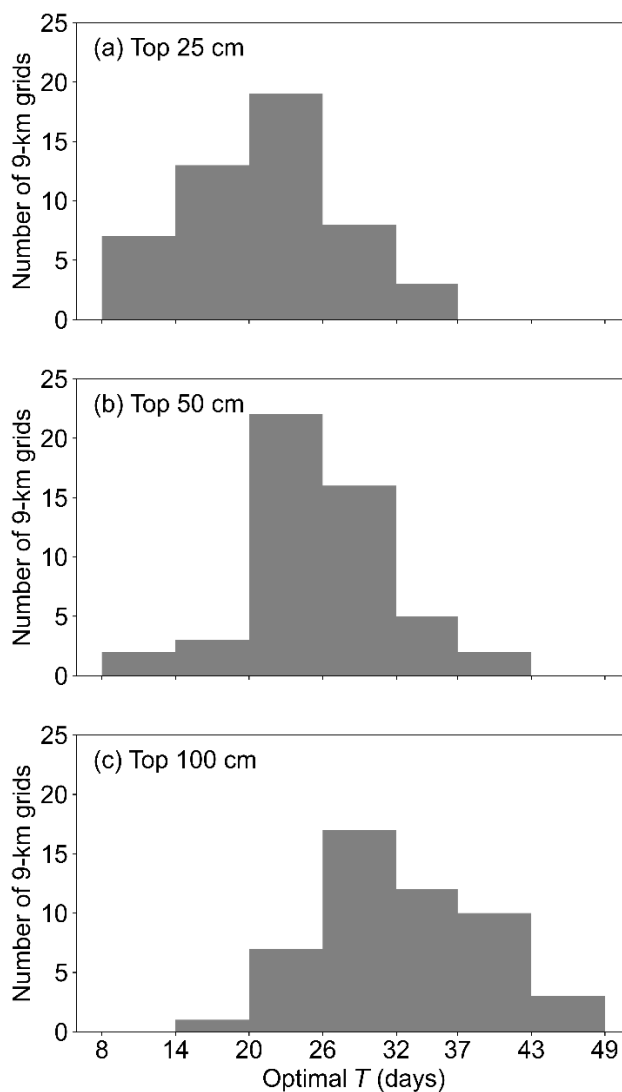
825



Figures A9: Left: (a) ubRMSD, (c) R , and (e) anomaly R between the SMAP-derived SWI ($T = 15$ days) and HGS simulated 0–25 cm soil moisture across all SMAP grids over the study watershed. Right: (b) ubRMSD, (d) R , and (f) anomaly R between the SMAP derived SWI ($T = 20$ days) and HGS simulated 0–100 cm soil moisture across all SMAP grids over the study watershed.



Figures A10: Left: Optimal T_{opt} for SWI estimation for (a) 0–25 cm, (c) 0–50 cm, and (e) 0–100 cm soil layers, respectively. Right: Maximum Spearman's rank correlation between the SWI and simulated soil moisture for (b) 0–25 cm, (d) 0–50 cm, and (f) 0–100 cm soil layers, respectively.



835

Figure A11: Distribution of the optimal T_{opt} at the 9-km grid scale for (a) 0–25 cm, (b) 0–50 cm, and (c) 0–100 cm soil depths, respectively.